Nano Research

ISSN 1998-0124 CN 11-5974/O4
https://doi.org/10.26599/NR.2026.94908940

Research Article

Rapid water purification enabled by balancing metal and non-metal electron transfer channels in peroxymonosulfate activation

Yuxuan Bai[1], Ganbing Zhang[2], Yetong Hua[1], Tiantian Hao[1], Zhaoyu Qiao[1], LiJuan Tian[1], Yi Shi[1], Hui Xu[1](✉)

[1] State Key Laboratory of Green Pesticide, Engineering Research Center of Photoenergy Utilization for Pollution Control and Carbon Reduction, Ministry of Education, College of Chemistry, Central China Normal University, Wuhan 430079 , China

[2] Collaborative Innovation Center for Advanced Organic Chemical Materials Co-constructed by the Province and Ministry, Ministry-of-Education Key Laboratory for the Synthesis and Applications of Organic Functional Molecules, College of Chemistry and Chemical Engineering, Hubei University, Wuhan 430062, China

Nano Res., **Just Accepted Manuscript** • https://doi.org/10.26599/NR.2026.94908940

https://www.sciopen.com/journal/1998-0124 on Jun. 16, 2026

Just Accepted

TABLE OF CONTENTS (TOC)

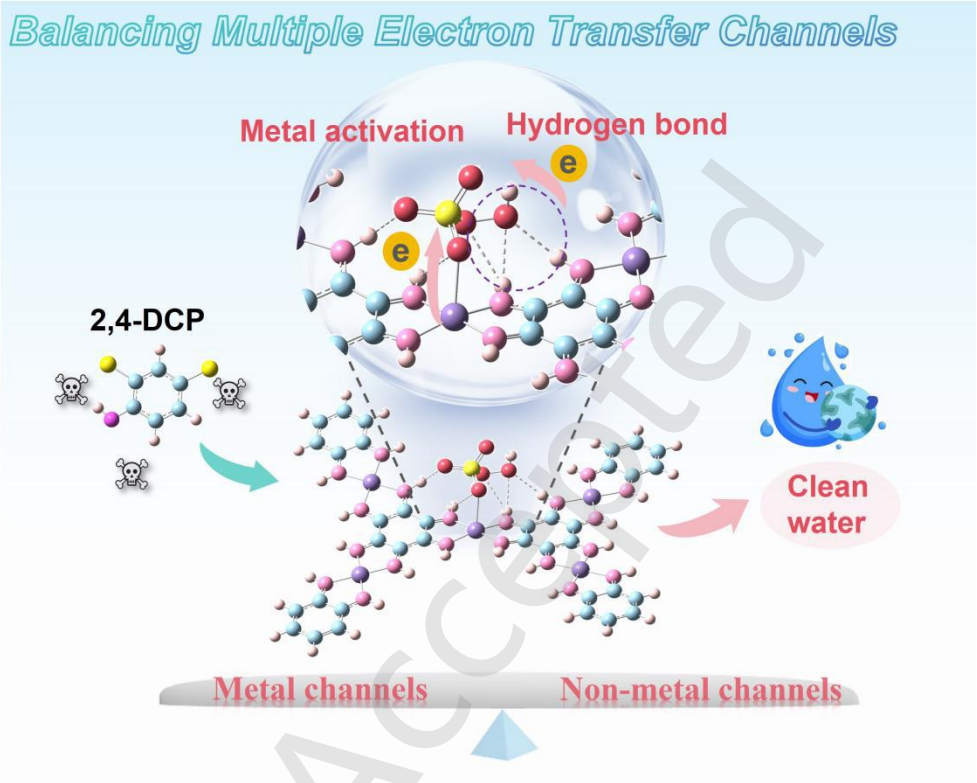

This work unveils a hydrogen-bonding-enhanced multi-channel electron transfer mechanism for PMS activation, strategically balancing metal-center adsorption with an extensive non-metallic hydrogen-bonding network within metal-organic frameworks. The resulting catalytic system achieves complete pollutant degradation within 30 seconds, demonstrating exceptional reaction kinetics and great promise for practical, high-efficiency water purification.

Nano Research

Open Access

Review Article/Research Article Please choose on

Rapid water purification enabled by balancing metal and non-metal electron transfer channels in peroxymonosulfate activation

Yuxuan Bai [1], Ganbing Zhang [2], Yetong Hua [1], Tiantian Hao [1], Zhaoyu Qiao [1], LiJuan Tian [1], Yi Shi [1], and Hui Xu [1]✉.

[1] *State Key Laboratory of Green Pesticide, Engineering Research Center of Photoenergy Utilization for Pollution Control and Carbon Reduction, Ministry of Education, College of Chemistry, Central China Normal University, Wuhan 430079 , China*
[2] *Collaborative Innovation Center for Advanced Organic Chemical Materials Co-constructed by the Province and Ministry, Ministry-of-Education Key Laboratory for the Synthesis and Applications of Organic Functional Molecules, College of Chemistry and Chemical Engineering, Hubei University, Wuhan 430062, China*

Received:16 March 2026; **Revised:** 27 May 2026; **Accepted:** 16 June 2026

✉Address correspondence to huixu@ccnu.edu.cn

Cite this article: *Nano Research*, 2026, 19, 94908940 https://doi.org/10.26599/NR.2026.94908940

ABSTRACT: Carbon-supported catalysts hold great promise in environmental remediation. While extensive attention has been paid to the role of transition metal centers, the electron transfer mediated by non-metallic components during peroxymonosulfate (PMS) activation has long been overlooked. In this work, a series of M-hexaaminobenzene (HAB) (M = Fe, Co, Cu) metal-organic frameworks were synthesized to investigate the essential roles of metal and non-metal constituents and their correlation with catalytic expression. In situ spectroscopic characterization and density functional theory calculations indicate that, beyond the electron interaction between metal centers and PMS, hydrogen atoms within the HAB ligands form multiple hydrogen bonds with the terminal oxygen atoms of PMS. The metal and non-metal channels work synergistically to promote PMS activation. Crucially, we further discovered that the optimal catalytic performance is achieved by effectively balancing these two pathways, which requires a moderate metal-PMS adsorption coupled with an extensive and strong hydrogen-bonding network. This work presents the first elucidation of the relationship between multi-channel electron transfer and catalytic activity. The resulting Co-HAB system exhibited remarkable decontamination performance, completely degrading 2,4-dichlorophenol within 30 seconds with an ultrahigh reaction rate constant of 9250 min^{-1} mol^{-1}. Moreover, continuous operation in a membrane flow reactor confirmed the high efficiency and stability of the M-HAB/PMS system in practical water treatment. This work pioneers the hydrogen bond-induced multi-channel electron transfer to intensify PMS activation, establishing a valuable design perspective for high-performance catalysts in advanced oxidation processes.

KEYWORDS: peroxymonosulfate • metal-organic frameworks • advanced oxidation processes (AOPs) • electron transfer process (ETP) • multi channels • catalyst

1. Introduction

Persistent organic contaminants in wastewater present substantial threats to sustainable water supply, human health and ecological security [1,2]. In recent years, peroxymonosulfate-based advanced oxidation processes (PMS-AOPs) have gained recognition as effective technology for water purification [3-5]. In the design of conventional Fenton-like catalytic systems, extensive research has focused on the singular regulation of the electronic structure of metal centers [6,7]. Strategies such as modulation of the coordination environment [8], heteroatom doping [9], and atomic defect engineering [10] have been employed to enhance catalytic activity. However, traditional catalytic systems primarily rely on a single-pathway PMS interaction, which inevitably suffers from limited electron cycling at localized active sites and inefficient charge carrier migration, leading to sluggish reaction kinetics. Moreover, these strategies may compromise the structural integrity of the catalyst, resulting in the loss of active sites [11,12]. In contrast, constructing dual-channel or multi-channel synergistic catalytic systems and establishing "electron highways" can significantly improve catalytic cycling efficiency, overcome the inherent limitations of metal-dependent reaction processes, and simultaneously enhance both activity and durability [13,14]. Recent studies have highlighted the critical role of dual-channel systems in catalytic regulation. For example, the synergy between cobalt sites and $[V_4O_{12}]^{4-}$ clusters markedly improved the degradation rate of ofloxacin by $Co_2([V_4O_{12}])(bpy)_2$, establishing an auxiliary electron transfer pathway independent of direct metal-PMS interaction [15]. The "multi-path collaboration and concerted action" design concept holds great promise for advancing Fenton-like reaction systems across multiple dimensions, including efficiency, applicability, and stability [16,17]. It is

noteworthy that research on utilizing dual-channel or multi-channel electron transfer mechanisms to promote PMS activation remains in its early stages. In particular, the development of universal catalysts capable of multi-path electron transfer, as well as the elucidation of the structure-activity relationships between channel characteristics and catalytic performance, still require in-depth exploration.

Metal-organic frameworks (MOFs), as versatile inorganic-organic hybrid materials, are characterized by well-defined structures and versatile design possibilities [18-20]. Especially, newly emerging hexaaminobenzene (HAB) could be used as organic linkers to construct special MOFs with unique properties [21,22]. Recently, a few two-dimensional (2D) π-conjugated MOF containing HAB were used in the fields of CO_2 reduction reaction, electrochemical capacitors and energy storage systems, benefiting from their high packing density and unique combination of electronic conduction [23,24]. Therefore, it is expected that the exceptionally high electron density and impressive conductivity of HAB-based MOF can act as an effective electron sink, thereby accelerating interfacial reaction kinetics and promoting electron transmission [25]. Importantly, the rich nitrogen and hydrogen sites in the HAB linker led us to hypothesize a non-metal activation mechanism during its interaction with asymmetrical PMS. Specifically, we propose that the terminal oxygen atom (O=O-) of PMS serves as a strong hydrogen-bond acceptor, engaging with hydrogen atoms from the -NH_2 groups in HAB to form N-H · · · O hydrogen bonds. However, to our knowledge, no studies have applied HAB-based MOFs as a platform to investigate multi-channel PMS activation and its structure-activity relationships in Fenton-like catalysis.

In this study, we synthesized a series of transition metal-hexaaminobenzene MOFs (M-HAB MOFs, M = Fe, Co, Cu) to establish three distinct multichannel catalytic systems for efficient pollutant degradation. Experimental results reveal that metal active sites facilitate PMS adsorption and activation, while hydrogen-bonding components simultaneously engage oxygen moieties in PMS to establish auxiliary electron-transfer pathways. Notably, we further discovered that the M-HABs with distinct metal centers exhibit divergent catalytic performance. In situ infrared spectroscopy and DFT calculations demonstrate that excessively strong metallic adsorption suppresses hydrogen-bond formation between organic ligands and PMS, thus impeding catalytic activity. Conversely, optimal catalytic performance occurs when the metallic pathway was moderately balanced with a robust non-metallic pathway, establishing a clear relationship between metal channels and non-metal channels and activation efficiency. Benefiting from complementary metal-centered and hydrogen-bonding pathways, all catalysts exhibit exceptional degradation activity. Remarkably, Co-HAB achieves ultra-rapid degradation of 2,4-dichlorophenol within 30 seconds, and the reaction kinetic constant reaches 9250 min^{-1} M^{-1}, which is 2-3 orders of magnitude higher than the relevant studies. Furthermore, the non-radical oxidation mechanism predominant in Co-HAB confers exceptional pH adaptability and robust performance in the presence of both cations and anions, as well as across various water qualities. Further, we developed a catalytic membrane reactor to evaluate its application potential. This work provides deep insights into the relationship between multi-channel electron transfer and catalytic efficiency, offering valuable guidance for the design of advanced catalysts in oxidative water purification.

2. Experimental

2.1. Chemicals and Materials

Detailed information used in this study is provided in Text S1 of the Supporting Information.

2.2. Preparation of the family of M-HAB catalysts

As for the synthesis of Co-HAB, $CoCl_2·6H_2O$ (55 mg, 0.23 mmol) and $NH_3·H_2O$ (1.4 mL) were added into degassed DMSO (3 mL). And the mixture was added to a degassed DMSO (3 mL) solution of HAB hydrochloride (40 mg) in a glass vial. After that, the vial was loosely covered and left for 6 hours at 65°C without stirring. The product precipitates out as a black solid. Filtered the mixture and washed the product once with acetone and twice with ionized water. The synthesis procedures for Fe-HAB and Cu-HAB were similar to that of Co-HAB, except that the metal salt was replaced with $FeCl_2·4H_2O$ (45.73 mg, 0.23 mmol) and $CuCl_2·2H_2O$ (39.22 mg, 0.23 mmol), respectively.

2.3. EPR experimental details

For the radical or high-valent metal-oxo species detection, 0.2 mM PMS, 0.05 g L^{-1} catalyst, and 200 μM DMPO were mixed in a test tube for 1 min. The mixed solution was then transferred into a capillary tube, which was then quickly inserted into the cavity of the EPR spectrometer to collect the EPR signal. The detection procedure of $^1O_2$ was the same as above, except using TEMP (200 μM) as a trapping agent. For the EPR spectra measurement of $O_2^{\bullet-}$, the procedure is similar to that of radical trapping experiments except for replacing water with methanol.

2.4. PMS concentration measurements

Residues PMS was determined as follows: 2 mL of the suspension was withdrawn at specified time intervals and filtered using a 0.22 μm polytetrafluoroethylene (PTFE) syringe filter. Then, 0.5 mL of reaction solution was taken and mixed with 4.5 mL of 1.11 g L^{-1} aqueous KI solution. The mixed solution was shaken for 20 min to ensure complete reaction between I- and HSO_5^- to form I_3^- (Eq. 1). The concentration of I_3^- was proportional to the PMS using a UV spectrophotometer (U-3900, Hitachi, Japan) measured at 352 nm [26].

$$2I^- + HSO_5^- + 2H^+ \rightarrow HSO_4^- + I_2 + H_2O$$

$$I_2 + I^- \rightarrow I_3^- \quad \text{(Eq. 1)}$$

2.5. More Experimental Procedures

A series of interference experiments involving anions, natural organic matter, initial pH, and natural waters were carried out to assess the environmental adaptability of the proposed system. The system' s generality was further confirmed by degradation experiments on various pollutants. Finally, the system's long-term stability was evaluated using a membrane reactor to examine its stability and practical applicability. Further details on analytical methods and experimental procedures are provided in Supporting Information.

3.Results and discussion

3.1. Characterizations of M-HAB

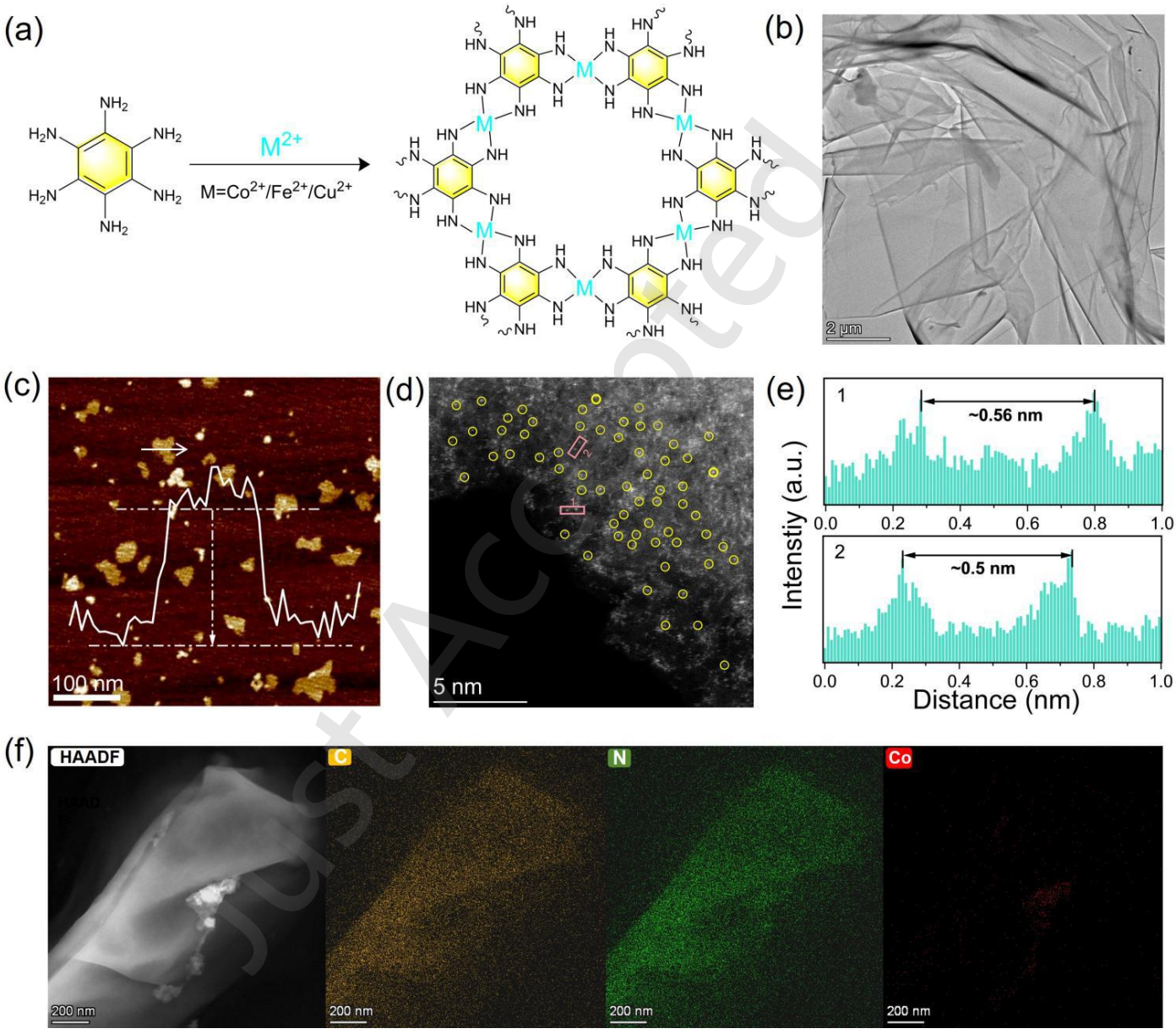

Fig. 1. (a) Illustration of the synthetic process for preparing Co-HAB; (b) TEM image; (c) AFM image and corresponding height profiles; (d) magnified AC-HAADF-STEM image; (e) The height profile of single-atom pairs marked in (d); (f) STEM-EDS mapping of Co-HAB.

The facile solvothermal reaction of the HAB ligand with Fe(Ⅱ), Co(Ⅱ), or Cu(Ⅱ) salts at 65 °C successfully yielded black microcrystalline powders of the corresponding M-HAB (M=Fe, Co, Cu) models [23]. A depiction of the M-HAB structure is displayed in **Fig. 1**a. Scanning electron microscopy (SEM) and transmission electron microscopy (TEM) images revealed that Co-HAB comprises stacked 2D nanosheets (Fig. 1b and **Fig. S**1). The lamellar morphology with a thickness of 3.12 nm was confirmed by the height profile of atomic force microscopy (**Fig.1**c). Atomically monodispersed bright spots are clearly observed by the aberration-corrected high-angle annular dark-field scanning transmission electron microscopic (AC-HAADF-STEM) images (**Fig. 1**d). The distance between adjacent bright spots in the AC-HAADF-STEM image was measured to be approximately 0.5 nm (as shown by the intensity profile) (**Fig. 1**e). This value is significantly larger than the typical Co-Co bond length (~0.25 nm) in metallic cobalt, precluding the existence of Co clusters or nanoparticles. This result

provides strong evidence that Co is atomically dispersed on the HAB support, stabilized by coordination with the nitrogen atoms of the organic framework. The relevant energy-dispersive spectroscopy (EDS) elemental mapping confirms the presence of well-dispersed Co, N, and C elements in Co-HAB, with uniformly-dispersed metal ions (**Fig. 1**f). Similar TEM and EDS results of morphology features were also obtained for Fe-HAB and Cu-HAB catalysts (**Figs. S**2 and **S**3). Fourier-transform infrared (FT-IR) analysis verified that the similar structural and physicochemical properties of the M-HAB catalysts (**Fig. S**4). The peaks are assigned to N-H stretch (3200-3500 cm^{-1}), aromatic C=C stretch (1602 cm^{-1}) and C-N stretch (1419 cm^{-1}). The metal contents of M-HAB catalysts ranged from 7.2 to 7.7 wt.%, according to the inductively coupled plasma optical emission spectrometry (ICP-OES) analysis (**Table S**1). The survey spectra of X-ray photoelectron spectroscopy (XPS) identified characteristic peaks of C, N, O and Fe/Co/Cu in the prepared materials (**Figs. S**5, **S**6 and **S**7). The high-resolution Co 2p spectrum (Fig. S5b) exhibits distinct satellite peaks characteristic of Co(II), while the main peak position and asymmetry suggest the coexistence of Co(III), indicating a mixed-valence state (Co(II)/Co(III)) for cobalt in the material. The high-resolution Fe 2p spectrum (**Fig. S**6b) shows that the main Fe $2p_{3/2}$ peak is located at 711 eV, accompanied by a satellite peak at approximately 718 eV, indicating that iron predominantly exists in the mixed-valence states of Fe(II)/Fe(III) oxidation states. In the Cu 2p spectrum (**Fig. S**7b), the main peaks of Cu $2p_{3/2}$ and Cu $2p_{1/2}$ appear at 934 eV and ~954 eV, respectively, along with satellite peaks (940 – 945 eV), suggesting that copper is primarily in a mixed Cu(I)/Cu(II) oxidation state within a coordination environment. The N 1s spectra for all three metals can be deconvoluted into two distinct peaks at binding energies of 398.3 eV and ~400.0 eV, corresponding to quinoid imine (=N-) and benzenoid amine (-NH-) species, respectively, which are in excellent agreement with the expected complex coordination structures in M-HAB.

3.2. Catalytic Effect Test

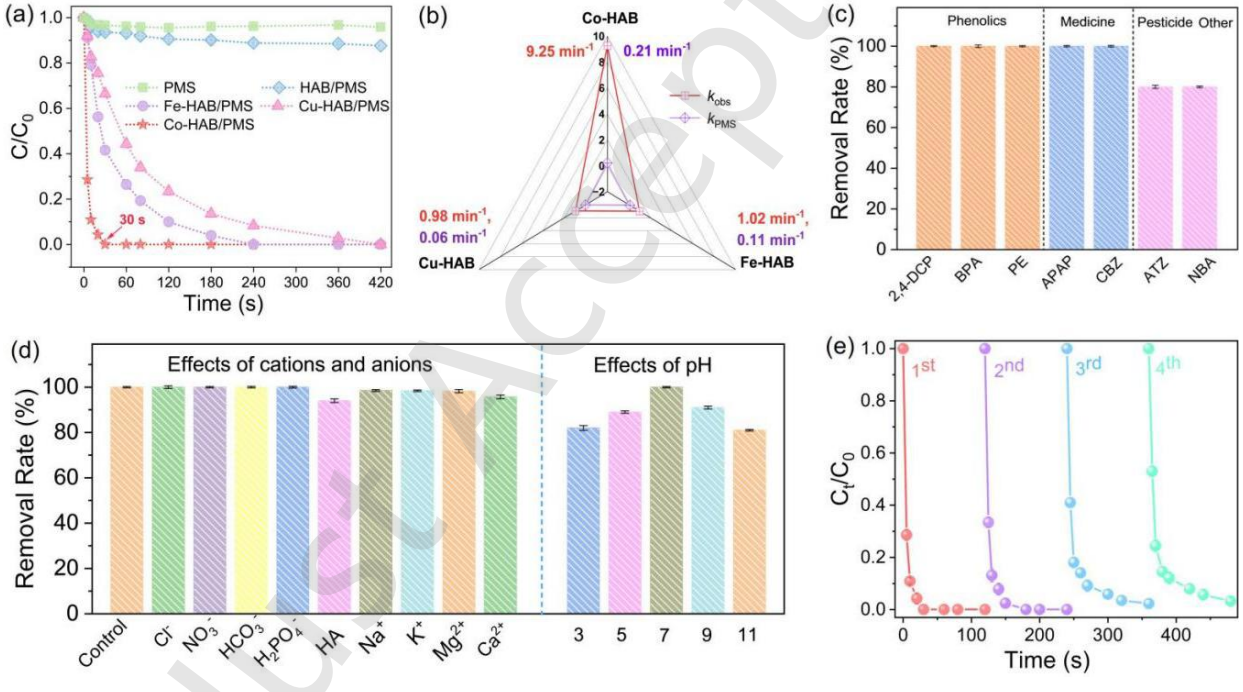

Fig. 2. Catalytic performance of M-HAB in PMS-assisted ROS production. (a) Degradation curves of 2,4-DCP within 420 s; (b) The k_{obs} and k_{PMS} in these catalysts/PMS systems; (c) Degradation rate of different model pollutants in Co-HAB system; (d) Effects of environmental background cations, anions, and natural organic matter on the Co-HAB/PMS system; Degradation rate under different initial pH environments; (e) Cycling experiments of the Co-HAB/PMS system. Experimental conditions: $[PMS]_0$ = 0.2 mM, $[Catalysts]_0$ = 0.05 g L^{-1}, $[pollutants]_0$ = 10 mg L^{-1}, [salts]= 50 mM, [HA]=10 mM, T = 25 °C.

The Fenton-like catalytic activity was assessed via PMS activation for 2,4-DCP degradation, a typical pesticide and pharmaceutical intermediate. As illustrated in **Fig.S**8, key parameter including PMS concentration, catalyst dosage, and reaction atmosphere were systematically optimized. Balancing degradation efficiency and reagent economy, the optimal conditions were established at 200 μM PMS and a catalyst loading of merely 0.05 g L^{-1}. Atmosphere comparison revealed negligible difference in removal efficiency between air- and N_2 saturated conditions, indicating that dissolved oxygen does not participate in the catalytic oxidation, further confirming that the reaction primarily relies on PMS-derived reactive species. The adsorption of the three M-HAB catalysts alone could remove about 18% of 2,4-DCP, the effect on high-speed catalytic degradation is negligible (**Fig. S**9). Specifically, Co-HAB, Fe-HAB, and Cu-HAB achieved ultra-rapid removal efficiencies within 30, 240, and 420 seconds, respectively (**Fig. 2**a). Co-HAB exhibited the highest PMS activation for 2,4-DCP degradation, achieving the largest apparent rate constant constant (k_{obs}) of 9.25 min^{-1} (**Fig. S**9d). This superior performance was further confirmed by PMS consumption experiments, which showed that Co-HAB consumed approximately 80% of the PMS within the given timeframe, demonstrating efficient oxidant utilization with an apparent rate constant k_{PMS} of 0.21 min^{-1} (**Figs. 2**b and **S**10). Much lower reactivity was observed by PMS or catalysts alone and

HAB/PMS controls. The homogeneous Fe^{2+}, Fe^{3+}, Co^{2+} or Cu^{2+} also have no performance on degrading 2,4-DCP (**Fig. S11**a). Furthermore, at an identical dosage of 0.05 g L^{-1}, the heterogeneous catalysts CoO, Co_3O_4, Fe_2O_3, and CuO achieved a degradation efficiency of less than 20% for 2,4-DCP (**Fig. S11**b). Furthermore, the complete inhibition on the degradation performance of the M-HAB+PMS system by the incorporation of KSCN as a chemical chelator to target metal sites further suggests the importance of M sites in heterogeneous catalysts for the activation of the PMS (**Fig. S**12) [27]. As shown in **Table S**3, the M-HAB/PMS systems deliver the highest k-value (the modification value of reaction rate constant), reaching up to 9250 $min^{-1}M^{-1}$, which is 2-3 orders of magnitude higher than other existing Fenton-like advanced systems. Furthermore, these systems demonstrated superior performance with lower dosages of both PMS and catalyst, fulfilling environmentally friendly ecological requirements and highlighting the advantages of HAB-based catalysts.

Further experiments on the degradation of an array of seven additional pollutants validated the broad-spectrum efficacy of Co-HAB. Within 4 min, various phenolic contaminants, medicine, as well as pesticide, including bisphenol A (BPA), phenol (PE), acetaminophen (APAP), and carbamazepine (CBZ) could be removed by nearly 100% (**Figs. 2**c and **S**13). While atrazine (ATZ) and 4-nitrobenzoic acid (NBA), a kind of compounds with electron-withdrawing properties, could be reduced by approximately 80%. This reactivity highlights Co-HAB ' s extraordinary selective for Fenton-like oxidation in targeting electron-rich pollutants, facilitated by the nonradicals-predominant pathway (**Fig. S**14) [28]. The solution matrix typically contains abundant cations, anions, and natural organic matter, notably humic acid (HA). It is therefore essential to evaluate the resistance of catalysts to interference from the actual water background. Experimental results demonstrate that common anions (Cl^-, NO_3^-, HCO_3^-, $H_2PO_4^-$), cations (Na^+, K^+, Mg^{2+}, Ca^{2+}) and natural organic matter did not lead to any significant loss in the activity of the Co-HAB catalyst, nor was the degradation rate substantially inhibited (**Figs. 2**c and **S**15). This highlights the system is minimally affected by common environmental matrices in real water bodies. Additionally, unlike the previously reported heterogeneous or MOFs-based catalysts, Co-HAB exhibited considerable pH resilience, operating effectively across a range from 3.0 to 11.0 (**Figs. 2**d and **S**16) [29]. Co-HAB demonstrated excellent reusability and water stability. Over 95% degradation efficiency was maintained after four cycles (**Fig. 2**e), while the Co leaching concentration remained below the Chinese Surface Water Environmental Quality Standard (GB 3838-2002, China) (0.2 mg L^{-1}, **Fig. S**17a,c) [30]. The contribution from leached homogeneous Co^{2+} in a single cycle was negligible (<13%), confirming the primarily heterogeneous catalytic pathway (**Fig. S**17b). All the results confirmed high efficiency and anti-interference activity of the Co-HAB/PMS process.

3.3. Reactive species generation pathway

To elucidate the oxidation regimes involved in three M-HAB systems, we conducted scavenging experiments to gain insights into it (**Figs. 3**a and **S**18). For all catalyst types, the addition of excess tert-butyl alcohol (TBA, a scavenger for •OH) [31] negligibly inhibited the removal efficiency, and the characteristic fluorescence emission spectrum peak at 460 nm was not detected by coumarin experiments, indicating the absence of •OH (**Fig. S**19). Additionally, the incorporation of p-benzo-quinone (p-BQ, $O_2^{\bullet-}$quencher) [26] had no obvious inhibitory effect, indicating that $O_2^{\bullet-}$ did not participate in degradation process. The absence of $O_2^{\bullet-}$ formation was further verified through nitrotetrazolium blue chloride method (**Fig. S**20). For the possible high-priced metal-oxygen (HVMO) species, it can selectively oxidize phenyl sulfoxide (PMSO) [32] to methyl phenyl sulfone products via an oxygen atom transfer mechanism, and thus PMSO will terminate the associated oxidation. As results, the addition of PMSO did not inhibit the removal efficiency, suggesting no generation of HVMO species. As a specific quencher of singlet oxygen ($^1O_2$), L-Histidine (L-His) significantly inhibited degradation. However, previous studies have pointed out that L-His can react with PMS, potentially leading to an overestimation of the contribution of $^1O_2$ [6,33]. To further investigate this, the solvent exchange (H_2O to D_2O) [34] did not enhance catalytic performance, suggesting that $^1O_2$ are not accountable for 2,4-DCP degradation (**Fig. S**21). Notably, methanol (MeOH, $SO_4^{\bullet-}$ quencher) [35] inhibited the degradation by all three catalysts to varying degrees, accompanied by a corresponding decrease in k_{obs} (**Fig. 3**a). This result indicates the involvement of $SO_4^{\bullet-}$ in the oxidation system, with varying yields and contributions of $SO_4^{\bullet-}$ observed across the Fe/Co/Cu-HAB catalytic systems (**Fig.3**b). Compared to •OH, $SO_4^{\bullet-}$ exhibit higher oxidative potential and longer half-lives [36]. Subsequently, the yield of $SO_4^{\bullet-}$ was determined using p-hydroxybenzoic acid as a probe [37]. As expected, and consistent with the quenching experiments, the highest $SO_4^{\bullet-}$ yield (19.8 μM) was observed with Cu-HAB, followed by Fe-HAB, with the lowest yield (7.2 μM) observed with Co-HAB. Nevertheless, MeOH incompletely inhibited the degradation of 2,4-DCP in the reaction systems, suggesting a contribution from an additional pathway, possibly direct electron transfer process (ETP) from the contaminant to PMS.

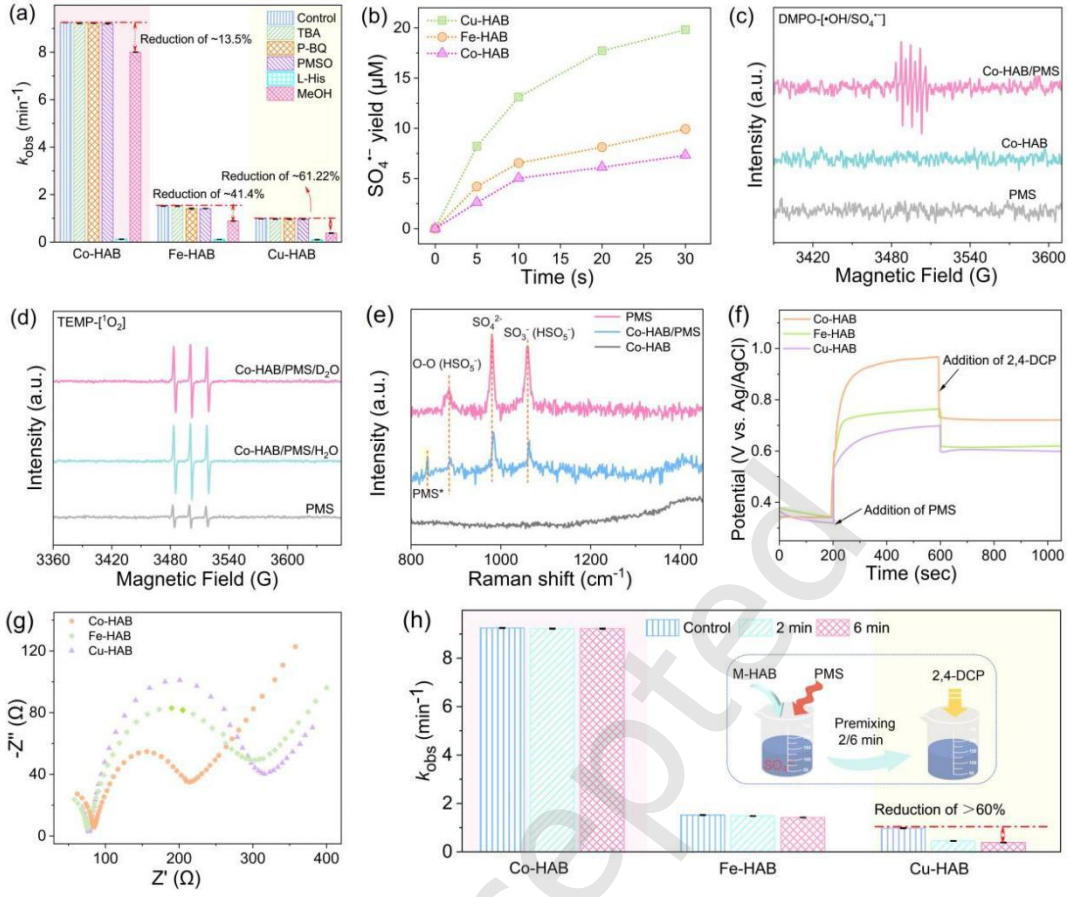

Fig. 3. (a) Effects of different scavengers on 2,4-DCP degradation kinetics; (b) Yield of $SO_4^{\bullet-}$ within 30 s; (c) DMPO-based EPR spectra; (d) TEMP-based EPR spectra; (e) In situ Raman spectra; (f) Variation of open-circuit potential for Co-HAB, Fe-HAB and Cu-HAB catalyst with addition of PMS and 2,4-DCP; (g) Electrochemical impedance spectroscopy of different catalysts; (h) The k_{obs} values of premixing test at designed time intervals. Experimental conditions: [2,4-DCP]=10 mg L^{-1}, [catalyst]=0.05 g L^{-1}, [PMS]=0.2 mM, [TBA]=[MeOH]=100 mM, [P-BQ]=[L-His]=5 mM, [PMSO]=10 mM.

EPR experiments with 5,5-dimethyl-1-pyrroline N-oxide (DMPO) and 2,2,6,6-tetramethylpiperidine (TEMP) as the spin-trapping agents were further conducted to directly identify the ROS [38]. **Fig. S**22 EPR spectra further rule out the contribution of $O_2^{\bullet-}$. As shown in **Fig. 3**c, no adducts of radicals were detected. Instead, the 5,5-dimethyl-1-pyrrolidone-N-oxyl (DMPOX) signal was observed, which is indicative of the direct oxidation of DMPO through non-radical mediated pathways [39], serving as supplementary evidence for the presence of ETP. The minor quartet characteristic peak of DMPO-$SO_4^{\bullet-}$ can be attributed to the overshadowing effect of the robust DMPOX signal [40]. As shown in **Fig. 3**d, triplet signals of 2,2,6,6-tetramethyl-4-piperidine-N-oxyl (TEMPO) were detected in the presence of PMS alone, resulting from the $^1O_2$ produced through the self-decomposition of PMS. Based on the above results, we verdict that TEMPO enhancement signals are derived from indicators of the complex-induced ETP on the catalyst surface. In this process, radical cations of TEMP (TEMP+•) are initially generated through single-electron extraction by excited peroxymonosulfate complex (PMS*), which then react with dissolved oxygen to form TEMPO [39,41].

During a typical ETP, PMS is initially surface adsorbed by catalysts to form surface-activated complexes with elevated oxidation potentials, enabling the extraction of electrons from the nucleophilic organic compounds. As ETP exhibits non-radical pathway characteristics by directly capturing electrons from contaminants, avoiding catalyst redox cycle and enabling efficient oxidant utilization [42]. In-situ Raman spectroscopy analysis was applied to probe the interaction of Co-HAB with PMS (**Fig. 3**e). The 880 cm^{-1} and 1060 cm^{-1} characteristic peaks represent the O-O (HSO_5^-) bond and SO_3^- (HSO_5^-), respectively, along with a characteristic peak of SO_4^{2-} at 980 cm^{-1} [43]. Upon the introduction of Co-HAB, a new characteristic peak positioned at 835 cm^{-1} appears, providing solid evidence for the formation of critical surface activated peroxide species (Co-HAB/PMS*) in the ETP regime. The gradually observed decline and red shifts of the two characteristic peaks of O-O and SO_3^-, are corresponding to the self-decomposition and consumption of PMS* [44]. The binding of contaminant (as electron donor) and oxidant (as electron acceptor) at the catalyst surface is essential for initiating ETP in Fenton-like catalysis. The detailed ETP pathway for 2,4-DCP degradation was further unveiled by timed open circuit potentials (OCPt) measurements. As shown in **Fig. 3**f, a remarkable increase in the catalyst potential following PMS injection into the electrolyte solution was observed and then it reached plateaus, corresponding to the immediate formation of surface activated complexes [45]. The stable potential of Co-HAB was 0.97 V, which was much higher than that of Fe-HAB (0.75 V) and Cu-HAB (0.69 V). It is reported that a strong positive correlation exists among the oxidation rate of ETP, the oxidation potential of the complexes, and the adsorption capacity of PMS. Consistent with the conclusions in **Figs. S**13,

Co-HAB consumes more PMS compared to Fe-HAB and Cu-HAB, indicating that Co-HAB exhibits the highest complexation capacity with PMS, which in turn results in the greatest oxidation potential and the fastest oxidation rate. Moreover, electrochemical impedance spectroscopy (EIS) measurements reveal that the semicircular diameter of Co-HAB indicates a charge transfer resistance significantly lower than that of Fe-HAB and Cu-HAB (**Fig. 3**g). This occurrence confirms Co-HAB's superior electrolyte penetration and reduced resistance, which contribute to its enhanced reaction kinetics. The decrease in the open-circuit potential upon introducing 2,4-DCP was ascribed to the electron-donating from the pollutant to the M-HAB/PMS* [46] facilitating the decomposition of surface complex (**Fig. 3**f). The amperometric i-t curve further supports this finding, demonstrating that the addition sequence of PMS and pollutants is crucial (**Fig. S**23). When PMS was first added into the electrochemical system, the current density of Co-HAB electrode was significantly increased. In contrast, when 2,4-DCP were first added to the electrochemical system, no current density change can be observed. The results of pre-mixing experiments demonstrated that as the pre-mixing time increased, the inhibition on 2,4-DCP degradation in Co-HAB and Fe-HAB remained minimal, indicating that the influence of ETP on pollutant oxidation overwhelmed that of $SO_4^{\bullet-}$ (**Figs. 3**h and **S**24). Conversely, $SO_4^{\bullet-}$ plays a dominant role in the degradation of 2,4-DCP within Cu-HAB/PMS system. **Fig. S**25 illustrates the relative contributions of ETP and $SO_4^{\bullet-}$ across all degradation systems.

3.4. Multi-channel electron transfer interaction mechanisms

DFT calculations were utilized to construct Co-HAB, Fe-HAB and Cu-HAB bulk models. PMS offers two types of O atoms for adsorption, a hydroxyl oxygen atom (OtypeI) and a terminal oxygen atom (O_{typeII}) (**Fig. S**26). As shown in **Fig. S**27, the interaction between M-HAB and the hydroxyl oxygen (O_{typeI}) of PMS is weak, with an excessively long distance between the metal and oxygen atoms, preventing the formation of a stable chemical bond. This observation is consistent with the experimental results presented in **Fig. 2**a, which demonstrate that pure HAB lacking a metal center cannot effectively activate PMS. Therefore, the metal-terminal oxygen atom represents the optimal adsorption model. We observed that the metal site in M-HAB binds to the OtypeII of PMS, while a multiple hydrogen bond forms between the terminal oxygen of PMS and the terminal hydrogen of HAB. Based on the optimal model, the Electron localization function-based core-valence bifurcation (ELF-based CVB) index was calculated for the three systems to evaluate the number and strength of hydrogen bonds [47]. Generally, a more negative CVB index corresponds to a stronger hydrogen bond. As illustrated in Fig. 4a, multiple hydrogen bonds were observed in all three materials: Co-HAB forms five relatively strong hydrogen bonds (with CVB values of 0.0483, 0.0573, 0.0603, 0.0627, and 0.0705), while Fe-HAB and Cu-HAB each form fewer hydrogen bonds, with only two identified. The adsorption energies between the metal centers and PMS were also evaluated. Fe-HAB exhibits excessively strong adsorption energy, which hinders the formation of additional hydrogen bonds (**Fig. 4**b). Although this results in stronger adsorption, the concomitant reduction in hydrogen bond formation leads to an overall decrease in catalytic activity compared to Co-HAB. In contrast, Cu-HAB shows excessively weak adsorption toward PMS; despite the presence of hydrogen bonds, it is unable to activate PMS efficiently. Owing to its optimal combination of the strong hydrogen bond network and moderate adsorption energy, Co-HAB demonstrates superior Fenton-like performance. These findings are illustrated in the volcano plot in **Fig. 4**b, in the multi-pathway electron transfer catalytic system, the metal pathway involves the interaction between PMS and the metal sites, while the non-metal pathway consists of a hydrogen-bonding network formed between the non-metallic components of M-HAB and PMS. When both the metal and non-metal pathways are weak, PMS cannot be stabilized on the material, leading to severely hindered activation and overall weak catalytic performance. When the metal pathway is too strong and the non-metal pathway is relatively weak, desorption is somewhat hindered [48], resulting in only moderate catalytic activity. The optimal catalytic performance is governed by a moderate metallic pathway working in concert with a strong non-metallic pathway. It indicates that this synergistic electronic interplay facilitates highly efficient PMS activation. Furthermore, as depicted in **Fig. 4**c, both the Co 3d and N 2p orbitals exhibit a significant blue shift, suggesting that PMS can attract electrons from both Co atoms and N(H) groups [15]. Similar situations could also be observed in Fe-HAB and Cu-HAB (**Fig. S**28). The formation of multiple weak hydrogen bonds facilitates interaction and electron transfer between the oxygen in PMS and the N-H groups in the material. On one hand, bonding electrons from the N-H bond are transferred to the vacant orbital of oxygen; on the other hand, electrons on oxygen are transferred to the antibonding orbital of the N-H bond. Both processes weaken the involved N-H bonds, which is structurally reflected in a slight elongation of these bonds after hydrogen bond formation (**Table S**4). Natural charge population analysis results (**Table S**5) reveal the electron gain and loss of O and H atoms in the PMS model after adsorption compared to the original PMS model. To investigate the crucial role of hydrogen bonding, a PMS adsorption model without hydrogen bonds was constructed and computed. As shown in **Figs. S**29-31, the positive adsorption energies (E_{ads}) for all models indicated the thermodynamically unfavorable adsorption.

To further confirm the pivotal role of hydrogen bonding, fluoride ions (F-, introduced as NaF) were added to compete with hydrogen atoms in HAB for hydrogen bond formation. The introduction of F- significantly suppressed the degradation efficiency of 2,4-DCP (**Fig. S**32), as F- tends to form strong hydrogen bonds with the O-H group in PMS, thereby reducing hydrogen bond formation between PMS and the catalyst. In situ FTIR spectroscopy was employed to further investigate the intermolecular interactions between PMS and Co-HAB during the PMS activation. The FTIR spectrum of an individual PMS molecule (**Fig. S**33) shows

peaks at 3607 cm^{-1} and 1100 cm^{-1}, corresponding to the O-H and S-O stretching vibrations, respectively [49]. Upon the addition of a certain concentration of catalyst, obvious blue shifts from 3607 cm^{-1} to 3450 cm^{-1} occurs for the O-H peak (**Fig. 4**d). After 30 seconds of reaction, the O-H peak remains at 3450 cm^{-1}, which attributed to the rapid consumption of PMS in the Co-HAB/PMS system. The dynamic shift of the O-H peak can be explained by: (i) strong interaction between the O-H group of PMS and the catalyst surface; and (ii) cleavage of the O-H bond in PMS due to the interaction, leading to the formation of a new stable O-H bond between the oxygen of PMS and the hydrogen at the HAB terminal on the catalyst surface. Furthermore, the projected density of states (PDOS) calculations revealed that the d-band center of Co-HAB is closer to the Fermi level than that of Cu-HAB, (**Fig. S**34) consistent with the experimental observations. A stronger interaction between Co-HAB and PMS leads to more efficient activation of PMS, especially when hydrogen bonds serve as additional electron transfer pathways and consequently enhancing pollutant degradation.

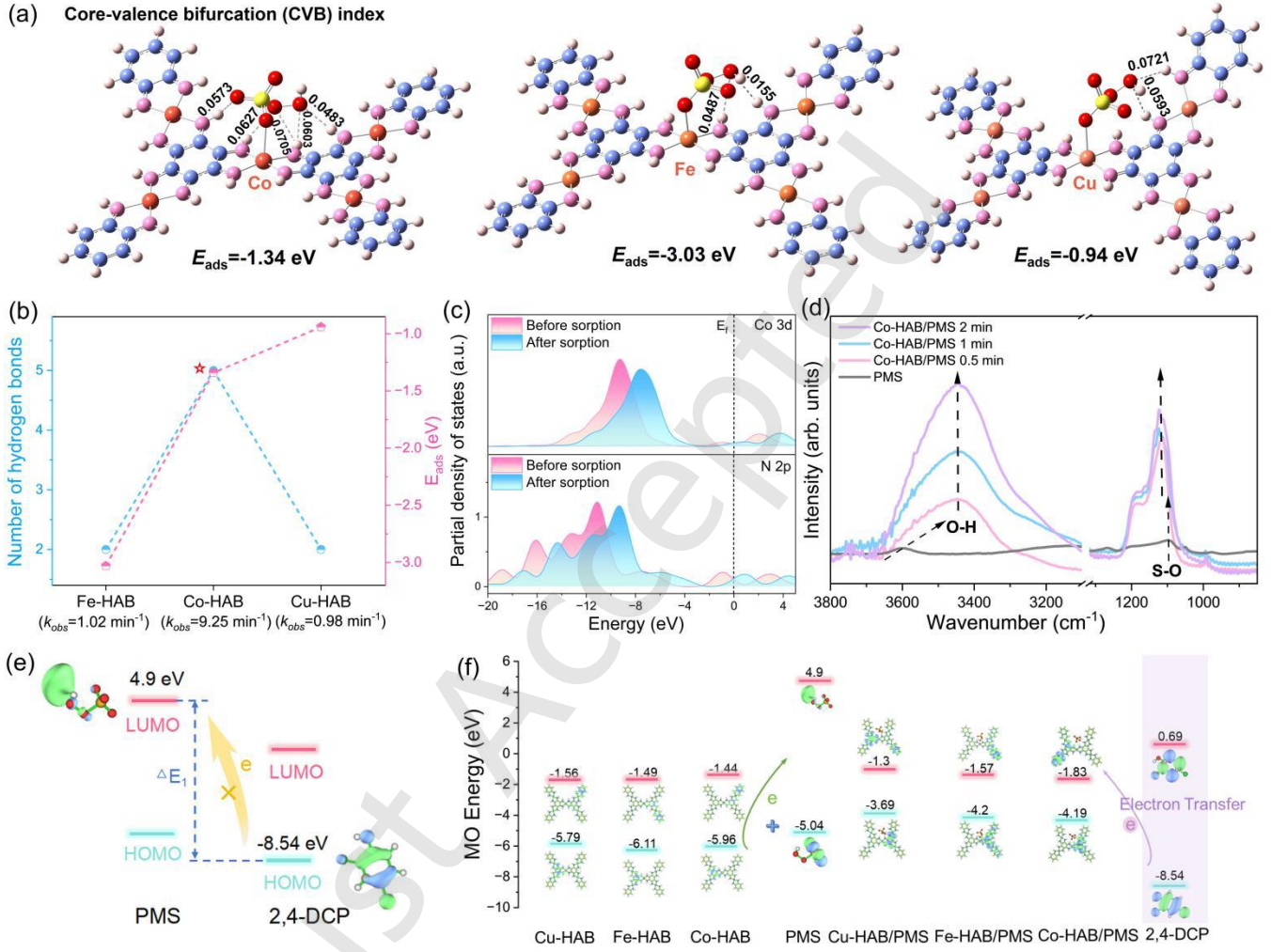

Fig. 4. (a) The core-valence bifurcation (CVB) index and adsorption energy calculations between PMS and Co-HAB, Fe-HAB and Cu-HAB; (b) The illustration relationship between hydrogen bonds, adsorption energy and catalytic performance; (c) PDOS of Co 3d and N 2p before and after PMS adsorption; (d) In situ FTIR spectra of Co-HAB/PMS system; Schematic diagram of the frontier orbital theory for (e) direct oxidation and (f) catalytic oxidation of 2,4-DCP.

The mechanism of 2,4-DCP removal by the catalyst was further elucidated using frontier orbital theory. Typically, direct reaction between 2,4-DCP and PMS requires electron transfer from the highest occupied molecular orbital (HOMO) of 2,4-DCP to the lowest unoccupied molecular orbital (LUMO) of PMS (**Fig. 4**e), which involves a high energy barrier (ΔE_1=13.44 eV). However, in the presence of a catalyst, a catalyst-oxidant complex is formed, which substantially reduces the energy gap. Notably, the HOMO (2,4-DCP)-LUMO(M-HAB/PMS*) gap is lowered to 6.71, 6.97 and 7.24 eV, for Co-, Fe- and Cu-HAB/PMS*, respectively. Moreover, the order of decreased energy barrier for electron transfer from 2,4-DCP (Co, Fe, and Cu) aligns well with the experimental results, further supporting the proposed electron transfer mechanism. This indicates that the complex formed on the catalyst surface can act as a highly efficient "electron absorber," capable of readily extracting electrons from the HOMO orbitals of pollutants, thereby facilitating the decomposition of PMS. Calculations of the frontier orbitals for the three materials, PMS, and 2,4-DCP (**Fig. 4**f) reveal that all catalysts contribute to a reduction in the energy gap. Since sulfate radicals are also involved in the oxidation reaction, the energy profiles for sulfate radical generation by the three materials were further computed. As shown in **Figs. S**35-37, Cu-HAB exhibits both thermodynamic and kinetic favorability for sulfate radical formation. In contrast, Co-HAB encounters a substantial energy barrier during this process, making $SO_4^{\bullet-}$ generation

less feasible, which is consistent with our earlier findings. Overall, it is demonstrated that the family of M-HAB catalysts activates PMS through a multi-channel electron transfer mechanism. The key mechanistic insights are summarized as follows: (1) Synergistic dual-channel activation: In addition to the metal-N_4 sites acting as electron donors to directly participate in PMS activation, the HAB organic ligands establish a critical hydrogen bonding network with PMS, which further enhances the adsorption and activation of PMS on the catalyst surface. (2) Balanced interfacial interactions: A moderate PMS adsorption energy on the metal sites is essential to ensure effective PMS anchoring without excessive binding. Concurrently, the robust non-metallic hydrogen bonding network synergistically promotes interfacial electron transfer. The equilibrium between these two factors constitutes the optimal catalytic interface. (3) Narrowed HOMO-LUMO gap: The synergistic effect between the metal centers and the hydrogen bonding network effectively reduces the energy gap between the HOMO of the pollutant 2,4-DCP and the LUMO of the catalyst-PMS complex, thereby facilitating the ETP. (4) Sustained catalytic cycling: The reactive complex formed on the catalyst surface subsequently extracts electrons from the pollutant. This process drives the oxidation of the pollutant while concurrently replenishing electrons to the metal centers, ensuring the continuity of the catalytic cycle.

3.5. Possible Degradation pathway analysis

The proposed degradation pathways of 2,4-DCP in the Co-HAB/PMS system were deduced by liquid chromatography-mass spectrometer (LC-MS) results (**Fig. S**38). The oxidation process of 2,4-DCP involves hydrogen transfer, de-chlorination, oxidation of phenolic hydroxyl groups, and a series of ring-cleavage reactions. [5,50] In pathway 1, the parasitic chlorine is initially attacked, yielding product P1, followed by an attack on the aromatic ring to generate product P2. Subsequently, P2 can be converted into either P3 or P4 through the interaction of H^+ with the aromatic structure. In pathway 2, the ETP directly initiates the de-chlorination of 2,4-DCP, resulting in the formation of P3 or P4, which can further undergo oxidation to produce the corresponding products P5, P6, or P7. Following this, the relatively reactive phenolic hydroxyl group in the structure is further oxidized and dechlorinated to yield products P8 and P9. Ultimately, the aromatic ring is cleaved into smaller organic acids, which can be readily converted into CO_2 and H_2O. The details of the intermediates are illustrated in **Fig. S**39. As indicated in **Fig. S**40, a total organic carbon (TOC) removal efficiency of 50.1%-67.2% was achieved in the three M-HAB/PMS systems. Advantageously, the continuous generation of small-molecule products with favorable microbial degradability in the M-HAB/PMS system enhances the potential for subsequent biochemical treatment of actual organic wastewater.

3.6. Practical decontamination applications

Meanwhile, the removal rates of contaminants could still reach 100% within 1 min in Yangtze water, East Lake water and tap water (**Fig. 5**a), indicating the strong antiinterference ability of the Co-HAB/PMS system in different aquatic environments. Exploring its application potential at a device level, M-HAB was integrated onto a commercially available organic PVDF membrane for continuously water purification in a membrane reaction unit (**Figs. 5**b and **S**41). The high porosity of PVDF surface enhanced the treatment capacity of the filter. The SEM images in **Fig. 5**c showed the porous surface and interconnected stacked structure in the catalytic membrane with an effective thickness of 70.1 μm and uniformly distributed C, N and Co elements. Benefiting from the abundant percolating channels and well-distributed metal elements within the membrane, the three continuous-flow catalytic systems maintained over 85% 2,4-DCP removal and the high water flux (45 L m^{-2} h^{-1} even after 700 h of operation, which were far exceed the performance of previously developed catalytic membranes (**Fig. 5**d) [51,52]. The superior stability originates from M-HAB's highly conjugated 2D planar structure, which firmly immobilizes active metal sites within its rigid framework to provide exceptional mechanical strength and effectively prevent metal leaching and agglomeration. Post-reaction samples were characterized using TEM and FT-IR. Comparative analysis with pre-reaction materials indicated no substantial alterations, confirming the structural stability of the synthesized catalyst (**Figs. S**42,43). This sustained stability highlights the catalyst's suitability for prolonged application in various catalytic processes. Overall, the wastewater treatment process constructed by M-HAB and PMS provides a green and sustainable path for sustainable water purification.

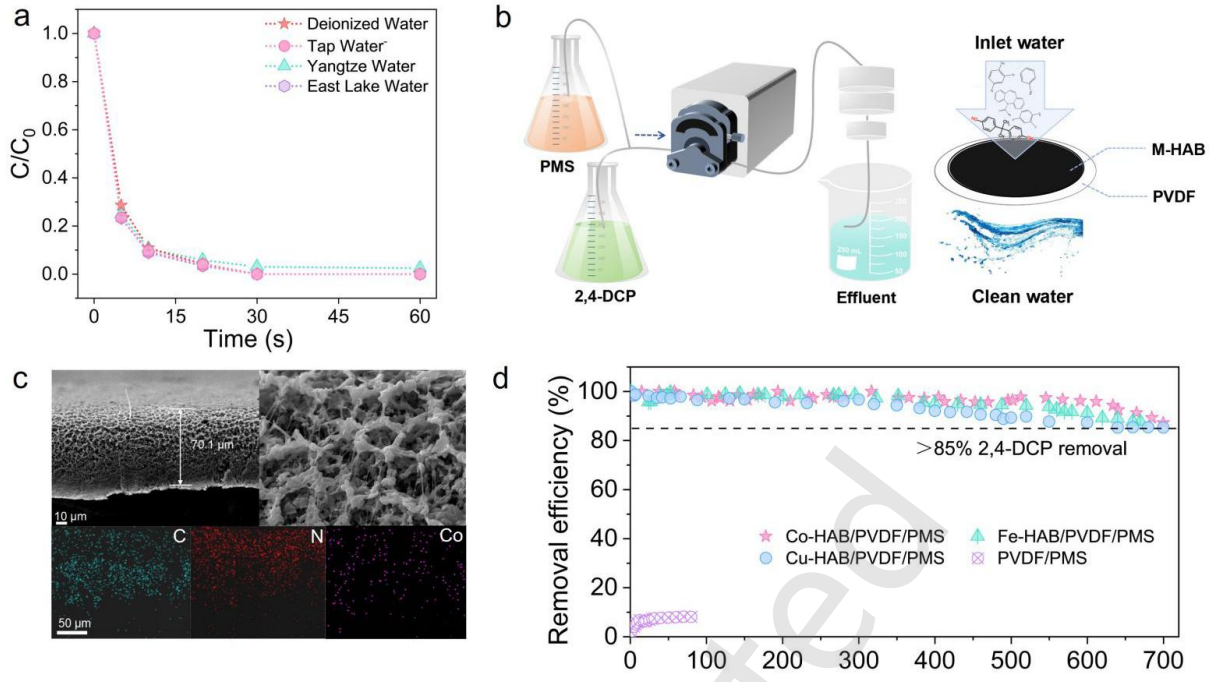

Fig. 5. (a) Degradation curves of 2,4-DCP in different natural waters; (b) The schematic diagram of the continuously flow filter; (c) Cross-sectional SEM images of the Co-HAB/PVDF membrane and its elemental mapping images; (d) Removal efficiency of 2,4-DCP in a continuous flow reactor system with different catalysts. Water quality information: Tap water: pH=7.7 ± 0.1, TOC=1.7 mg L^{-1}, Cl^-=55 mg L^{-1}; Yangtze River water: pH=7.4 ± 0.3, TOC=3.3 mg L^{-1}, Cl^-=49 mg L^{-1}; East Lake water: pH=7.8 ± 0.2, TOC=4.9 mg L^{-1}, Cl^-=34 mg L^{-1}.

4.Conclusion

In conclusion, this work presents a rationally designed M-HAB/PMS system that enables PMS activation through dual-pathways synergy and multi-channel electron transfer. The metal centers directly participate in PMS coordination, while the HAB ligands form a critical hydrogen-bonding network, collectively enhancing PMS adsorption and activation. DFT calculations reveal that moderate metal-PMS adsorption energy and the hydrogen-bonding network synergistically narrow the HOMO-LUMO gap between 2,4-DCP and the catalyst-PMS complex, thermodynamically favoring the electron transfer pathway. Notably, the metal centers impart pathway selectivity: Cu-HAB favors $SO_4^{\bullet-}$ radical generation, while Co-HAB preferentially drives ETP-mediated oxidation. This divergence further underscores that an effective balance between the metal-centered pathway and the non-metallic hydrogen-bonding network is the key to achieving high catalytic efficiency. Furthermore, the catalysts exhibit excellent stability, maintaining robust performance in complex water matrices and over 700 hours of continuous operation, underscoring their practical potential. This work establishes a new paradigm for designing efficient, durable heterogeneous Fenton-like catalysts through the synergistic integration of metal centers and organic ligand hydrogen-bonding networks.

Data availability

Data will be made available on request.

Acknowledgements

The authors gratefully acknowledge the financial support by the National Natural Science Foundation of China (No. 22576077,22076059).

Declaration of competing interest

The authors declare no competing financial interest.

Author contribution statement

Yuxuan Bai: Investigation, Data curation, Writing original draft, Validation, Methodology. Ganbing Zhang: Software, Methodology, Conceptualization. Yetong Hua: Investigation. Visualization. Tiantian Hao: Formal analysis, Visualization. Zhaoyu Qiao: Data curation. LiJuan Tian: Investigation. Yi Shi: Investigation. Hui Xu: Resources, Supervision, Conceptualization, Funding acquisition, Project administration, Writing-review & editing. All the authors have approved the final manuscript.

References

[1] Chen, Z.; An, F.; Zhang, Y.; Liang, Z.; Liu, W.; Xing, M. Single-atom Mo-Co catalyst with low biotoxicity for sustainable degradation of high-ionization-potential organic pollutants. *Proc. Nat. Acad. Sci.* 120 (**2023**) e2305933120.

[2] Mao, J.; Li, H.; Xu, Y.; Zhang, K.; Wang, Q.; Yang, L.; Gu, Z.; Bai, Y.; Lang, X.; An, X.; Qu, J. Enhanced photosynthetic electron transfer in microalgae-conjugated microporous polymer biohybrid: Unraveling mechanisms for high-efficiency water decontamination. *Appl. Catal. B-Environ.* 381 (2026) 125862.

[3] Gu, C.-H.; Pan, Y.; Wei, T.-T.; Zhang, A.-Y.; Si, Y.; Liu, C.; Sun, Z.-H.; Chen, J.-J.; Yu, H.-Q. Upcycling waste sewage sludge into superior single-atom Fenton-like catalyst for sustainable water purification. *Nat. Water*, 2 (**2024**) 649-662.

[4] Yang, T.; Chen, M.; Li, J.; Feng, Z.; Zou, S.; Mao, S.; Tian, Z.; Zhao, H. One Heterogeneous Catalyst Drives Two Selective Fenton-like Reaction Modes for Sustainable Water Decontamination. *Environ. Sci. Technol.* 59 (**2025**) 8155-8166.

[5] Zhu, Z.-S.; Wang, Y.; Wang, P.; Zhong, S.; Hu, K.; Ren, S.; Vongsvivut, J. P.; Sun, H.; Duan, X.; Wang, S. Multidimensional engineering of single-atom cobalt catalysts for ultrafast Fenton-like reactions. *Nat. Water*, 3 (**2025**) 211-221.

[6] Liu, S.; Du, J.; Wang, H.; Jia, W.; Wu, Y.; Qi, P.; Zhan, S.; Wu, Q.; Ma, J.; Ren, N.; Guo, W.-Q. How hetero-single-atom dispersion reconstructed electronic structure of carbon materials and regulated Fenton-like oxidation pathways. *Water Res*. 254 (**2024**)121417.

[7] Mo, F.; Song, C.; Zhou, Q.; Xue, W.; Ouyang, S.; Wang, Q.; Hou, Z.; Wang, S.; Wang, J. The optimized Fenton-like activity of Fe single-atom sites by Fe atomic clusters-mediated electronic configuration modulation. *Proc. Nat. Acad. Sci.* 120 (**2023**) e2300281120.

[8] Deng, Y.; Zhou, Y.; Song, Z.; Yang, X. Long-Range Electronically Polarized Fe-N_5 Catalysts Redirect Polymerization-Driven Phenolic Pollutant Removal Toward Sustainable Carbon Sequestration. *Angew. Chem. Int. Ed*. 64 (**2025**) e202509493.

[9] Long, Y.; Cao, Z.; Wu, W.; Liu, W.; Yang, P.; Zhan, X.; Chen, R.; Liu, D.; Huang, W. Rational modulation of Fe single-atom electronic structure in a Fe-N_2B_4 configuration for preferential $^1O_2$ generation in Fenton-like reactions. *Appl. Catal. B-Environ.* 344 (**2024**) 123643.

[10] Chen, Y.; Li, Q.; Su, R.; Gao, Y.; An, N.; Rong, Y.; Xu, X.; Ma, D.; Wang, Y.; Gao, B. Oxygen vacancies-mediated the peracetic acid activation to selectively generate $^1O_2$ for water decontamination. *Water Res*. 282 (**2025**) 123765.

[11] Song, Z.; Xu, J.; Zhang, L.; He, C.; Westerhoff, P.; Yang, X. Tailoring bidirectional electronic transfer interaction tunnels triggers sustainable and high activity of ozone catalysis for water purification. *Nat. Commun.* 16 (**2025**) 8121.

[12] Chen, T.; Zhang, G.; Sun, H.; Hua, Y.; Yang, S.; Zhou, D.; Di, H.; Xiong, Y.; Hou, S.; Xu, H.; Zhang, L. Robust Fe-N_4-C_6O_2 single atom sites for efficient PMS activation and enhanced Fe^{IV} = O reactivity. *Nat. Commun*. 16 (**2025**) 2402.

[13] Wang, H.; Zhou, F.; Wei, S.; Li, M.; Li, J.; Huang, J.; Liu, Y.-N. Rational construction of dual-charge transfer channels in imine covalent organic frameworks for enhanced photocatalytic performance. *Appl. Catal. B-Environ*. 384 (**2026**) 126234.

[14] Jiang, J.; Wu, J.; Yang, C.; Bo, S.; Zhang, J.; Li, B.; Zhang, Y.; An, Q.; Chen, X.; Liu, Q.; Zhou, W. Dynamically Dual-Center Coupled Synergistic Catalysis for Highly Efficient Oxygen Reduction. *Angew. Chem. Int. Ed*. 64 (**2025**) e202510188.

[15] Lan, M.-Y.; Li, Y.-H.; Wang, C.-C.; Li, X.-J.; Cao, J.; Meng, L.; Gao, S.; Ma, Y.; Ji, H.; Xing, M. Multi-channel electron transfer induced by polyvanadate in metal-organic framework for boosted peroxymonosulfate activation. *Nat. Commun*. 15 (**2024**) 7208.

[16] Fan, M.; Zhang, T.; Gao, Z.; You, S.; Shang, Y.; Peng, X.; Geng, L.; Wang, Y.; Liu, M.; Xu, X. Synergistic Architectures in Fenton-Like Catalysis: Bridging Single-Atom and Nanoparticle/Cluster Dynamics for Enhanced Activity, Stability, and Selectivity. *Adv. Funct. Mater.* 35 (**2025**) 2508484.

[17] Liu, Z.; Xu, X.-Y.; Xu, F.; Su, R.-D.; Li, B.; Zhang, F.; Xu, X.; Wang, Y.; Ma, D.-F.; Gao, B.-Y.; Li, Q. Diatomic "catalytic/co-catalytic" Fe/Mo catalysts promote Fenton-like reaction to treat organic wastewater through special interfacial reaction enhancement mechanism. *Water Res.* 274 (**2025**) 123147.

[18] Liu, M.; Wen, J.; Xiao, R.; Tan, R.; Qin, Y.; Li, J.; Bai, Y.; Xi, M.; Yang, W.; Fang, Q.; Hu, L.; Gu, W.; Zhu, C. Improving Interface Matching in MOF-on-MOF S-Scheme Heterojunction through π–π Conjugation for Boosting Photoelectric Response. *Nano Lett.* 23 (**2023**) 5358-5366.

[19] Cheng, M.; Lai, C.; Liu, Y.; Zeng, G.; Huang, D.; Zhang, C.; Qin, L.; Hu, L.; Zhou, C.; Xiong, W. Metal-organic frameworks for highly efficient heterogeneous Fenton-like catalysis. *Coord. Chem. Rev*. 368 (**2018**) 80-92.

[20] He, B.; Zhang, Q.; Pan, Z.; Li, L.; Li, C.; Ling, Y.; Wang, Z.; Chen, M.; Wang, Z.; Yao, Y.; Li, Q.; Sun, L.; Wang, J.; Wei, L. Freestanding Metal-Organic Frameworks and Their Derivatives: An Emerging Platform for Electrochemical Energy Storage and Conversion. *Chem. Rev.* 122 (**2022**) (11), 10087-10125.

[21] Dou, J.-H.; Sun, L.; Ge, Y.; Li, W.; Hendon, C. H.; Li, J.; Gul, S.; Yano, J.; Stach, E. A.; Dincă, M. Signature of Metallic Behavior in the Metal-Organic Frameworks M_3(hexaiminobenzene)$_2$ (M= Ni, Cu). *J. Am. Chem. Soc.* 139 (**2017**) 13608-13611.

[22] Hinckley, A. C.; Park, J.; Gomes, J.; Carlson, E.; Bao, Z. Air-Stability and Carrier Type in Conductive M_3(Hexaaminobenzene)$_2$, (M = Co, Ni, Cu). *J. Am. Chem. Soc*. 142 (**2020**) 11123-11130.

[23] Zhao, Z.-H.; Huang, J.-R.; Liao, P.-Q.; Chen, X.-M. Highly Efficient Electroreduction of CO_2 to Ethanol via Asymmetric C-C Coupling by a Metal-Organic Framework with Heterodimetal Dual Sites. *J. Am. Chem. Soc.* 145 (**2023**) 26783-26790.

[24] Feng, D.; Lei, T.; Lukatskaya, M. R.; Park, J.; Huang, Z.; Lee, M.; Shaw, L.; Chen, S.; Yakovenko, A. A.; Kulkarni, A.; Xiao, J.; Fredrickson, K.; Tok, J. B.; Zou, X.; Cui, Y.; Bao, Z. Robust and conductive two-dimensional metal-organic frameworks with exceptionally high volumetric and areal capacitance. *Nat. Energy* 3 (**2018**) 30-36.

[25] Park, J.; Lee, M.; Feng, D.; Huang, Z.; Hinckley, A. C.; Yakovenko, A.; Zou, X.; Cui, Y.; Bao, Z. Stabilization of Hexaaminobenzene in a 2D Conductive Metal-Organic Framework for High Power Sodium Storage. *J. Am. Chem. Soc*. 140 (**2018**) 10315-10323.

[26] Zhang, L.; Qi, J.; Chen, W.; Yang, X.; Fang, Z.; Li J.; Li, X.; Lu, S.; Wang, L. Constructing Hollow Multishelled Microreactors with a Nanoconfined Microenvironment for Ofloxacin Degradation through Peroxymonosulfate Activation: Evolution of High-Valence Cobalt-Oxo Species. *Environ. Sci. Technol.* 57 (**2023**) 42.

[27] Bai, Y.; Zhang, G.; Liu, M.; Hou, S.; Zheng, S.; Yang, S.; Zhu, C.; Xu, H. Spatial axial oxygen coordination of Co_{SA}-N_2O_1/MXene single-atom catalyst with electron-depleted active site for selective $^1O_2$ generation. *Appl. Catal. B-Environ*. 374 (**2025**) 125378.

[28] Jin, S.; Tan, W.; Huang, Y.; Wang, Y.; He, Z.; Zhang, H.; Song, S.; Cai, Y.; Zeng, T. Remote tuning of single-atom Fe-N_5 sites via high-coordination defects for enhanced Fenton-like water decontamination. *Nat. Commun*. 16 (**2025**) 10455.

[29] Gu, A.; Wang, P.; Chen, K.; Djam Miensah, E.; Gong, C.; Jiao, Y.; Mao, P.; Chen, K.; Jiang, J.; Liu, Y.; Yang, Y. Core-shell bimetallic Fe-Co MOFs to activated peroxymonosulfate for efficient degradation of 2-chlorophenol. *Sep. Purif. Technol*. 298 (**2022**) 121461.

[30] Ye, J.; Yu, C.; Dai, J.; Li, L.; Zhang, R.; Pan, J.; Xue, W.; Jiang, Y.; Zhao, J. Nanoconfined Cu-O-Mo Asymmetric Sites Enable Ambient Spontaneous O_2-to-$^1O_2$ Conversion for Sustainable Water Purification. *Adv. Mater*. (**2025**) e14600.

[31] Miao, F.; Wang, C.; Cheng, T.; Liu, Y.; Wang, R.; Duan, X.; Jiao, W. Carbon vacancy engineering regulates the cobalt-single-atom site for Co (IV)=O efficient generation and its ultrafast degradation of electron-rich pollutants. *Water Res.* 289 (**2026**) 124998.

[32] Chen, C.; Zhao, Y.; Zhang, K.; Li, Y.; Wu, Q.; Mao, K.; Wu, X.-L.; Su, J.; Zhang, H. Fluorine-induced spin-state tuning in Co_3O_4 enhances nonradical peroxymonosulfate activation efficiency. *Appl. Catal. B-Environ*. 378 (**2025**) 125574.

[33] He, Y.-L.; He, C.-S.; Lai, L.-D.; Zhou, P.; Zhang, H.; Li, L.-L.; Xiong, Z.-K.; Mu, Y.; Pan, Z.-C.; Yao, G.; Lai, B. Activating peroxymonosulfate by N and O co-doped porous carbon for efficient BPA degradation: A re-visit to the removal mechanism and the effects of surface unpaired electrons. *Appl. Catal. B-Environ*. 314 (**2022**) 121390.

[34] Qi, D.; Wang, J.; Zhang, J.; Su, K.; Xu, J.; Lv, W.; Wang, Y.; Zhang, Z.; Xiao, Y. Improving Generation Performance of $^1O_2$ by Atomic Doping for Efficient Catalytic Advanced Oxidation Processes. *Adv. Funct. Mater.* 34 (**2024**) 2406470.
[35] Liu, H.-Z.; Shu, X.-X.; Huang, M.; Wu, B.-B.; Chen, J.-J.; Wang, X.-S.; Li, H.-L.; Yu, H.-Q. Tailoring d-band center of high-valent metal-oxo species for pollutant removal via complete polymerization. *Nat. Commun*. 15 (**2024**) 2327.
[36] Wang, Y.; Li, D.; Ge, X.; Yu, J.; Zhao, Y.; Bu, Y. Anchored Cobalt Nanoparticles on Layered Perovskites for Rapid Peroxymonosulfate Activation in Antibiotic Degradation. *Adv. Mater*. 36 (**2024**) 2402935.
[37] Hu, J.; Gong, H.; Fu, K.; Jia, J.; Zhu, N. Overcoming metals redox rate limitations in spinel oxide-driven Fenton-like reactions via synergistic heteroatom doping and carbon anchoring for efficient micropollutant removal. *Water Res*. 261 (**2024**) 122020.
[38] Zhang, M.; Ding, J.; Li, G.; Peng, G.; Xiong, K.; Li, X.; Lang, X. Synergistic regulation of charge separation and enhanced adsorption in polarized covalent organic frameworks for photocatalytic degradation of an antibiotic pollutant. *Appl. Catal. B-Environ.* 391 (**2026**) 126639.
[39] Zhu, Z.; Wang, Y., Duan, X.,Wang, P., Zhong, S., Ren, S., Xu, X., Gao, B., Vongsvivut, J., Wang, S. Atomic-Level Engineered Cobalt Catalysts for Fenton-Like Reactions: Synergy of Single Atom Metal Sites and Nonmetal-Bonded Functionalities. *Adv. Mater.* 36 (**2024**) 2401454.
[40] Wu, Z.; Xiong, Z.; Liu, W.; Liu, R.; Feng, X.; Huang, B.; Wang, X.; Gao, Y.; Chen, H.; Yao, G.; Lai, B. Active Center Size-Dependent Fenton-Like Chemistry for Sustainable Water Decontamination. *Environ. Sci.Technol*. 57 (**2023**) 21416-21427.
[41] Tang, Q.; Wu, B.; Huang, X.; Ren, W.; Liu, L.; Tian, L.; Chen, Y.; Zhang, L.-S.; Sun, Q.; Kang, Z.; Ma, T.; Zou, J.-P. Electron transfer mediated activation of periodate by contaminants to generate $^1O_2$ by charge-confined single-atom catalyst. *Nat. Commun*. 15 (**2024**) 9549.
[42] Chen, Y.; Li, X.; Jiang, Z.; Yang, J.; Wang, Z.; Zhu, M. Ultralow H_2O_2-Triggered Electron Transfer over Single-Atom Iron Catalysts for Long-Term Recyclable Fenton-Like Reactions. *Angew. Chem. Int. Ed*. (**2025**) e23077.
[43] Yin, K.; Peng, L.; Chen, D.; Liu, S.; Zhang, Y.; Gao, B.; Fu, K.; Shang, Y.; Xu, X. High-loading of well dispersed single-atom catalysts derived from Fe-rich marine algae for boosting Fenton-like reaction: Role identification of iron center and catalytic mechanisms. *Appl. Catal. B-Environ*. 336 (**2023**) 122951.
[44] Miao, J.; Zhu, Y.; Lang, J.; Zhang, J.; Cheng, S.; Zhou, B.; Zhang, L.; Alvarez, P. J. J.; Long, M. Spin-State-Dependent Peroxymonosulfate Activation of Single-Atom M-N Moieties via a Radical-Free Pathway. *ACS Catal*. 11 (**2021**) 9569-9577.
[45] Yin, K.; Xu, X.; Yue, Q.; Shang, Y.; Li, Y.; Gao, Y.; Gao, B. Pore modulation of single atomic Fe sites for ultrafast Fenton-like chemistry with amplified electron migration oxidation. *Water Res*. 268 (**2025**) 122545.
[46] Wu, Y.; Zhao, K.; Wu, S.; Su, Y.; Yu, H.; Qian, X.; Shi, X.; Liu, A.; Huo, S.; Li, W.-W.; Niu, J. Fundamental Insights into the Direct Electron Transfer Mechanism on Ag Atomic Cluster. *Environ. Sci.Technol.* 58 (**2024**) 20699-20709.
[47] Fuster, F.; Silvi, B. Does the topological approach characterize the hydrogen bond? *Theor. Chem. Acc*. 104 (**2000**) 13-21.
[48] Li, X.; Huang, X.; Xi, S.; Miao, S.; Ding, J.; Cai, W.; Liu, S.; Yang, X.; Yang, H.; Gao, J.; Wang, J.; Huang, Y.; Zhang, T.; Liu, B. Single Cobalt Atoms Anchored on Porous N-Doped Graphene with Dual Reaction Sites for Efficient Fenton-like Catalysis. *J. Am. Chem. Soc*. 140 (**2018**)12469-12475.
[49] Ling, C.; Li, M.; Li, H.; Liu, X.; Zhan, G.; Sun, H.; Liang, C.; Li, Y.; Zhou, B.; Zhao, J.; Zhang, L. Symmetry dependent activation and reactivity of peroxysulfates on FeS_2(001) surface. *Sci. Bull.* 69 (**2024**) 154-158.
[50] Zhang, S.; Lu, Z.; Hu, C.; Li, F. Understanding the Distance Effect of the Single-Atom Active Sites in Fenton-Like Reactions for Efficient Water Remediation. *Adv. Sci*. 11 (**2024**) 2307151.
[51] Wang, X.; Li, T.; Fan, Z.; Duan, P.; Wang, L.; Pan, J.; Gao, B. Redox potentials of sulfonamide antibiotics mediating the electron transfer process in single-atom Cu catalyst/peroxymonosulfate system: Selective removal mechanisms for sulfonamides. *J. Hazard. Mater*. 485 (**2025**)136880.
[52] Chen, F.; Zhao, R.; Zhao, H.; Liu, Q.; Zhao, S.; Li, N.; Shen, Z.; Bu, X.-H. Axial Co-O-Cu Pairs Enable Superexchange Interaction for Efficient Co^{IV}=O Formation toward Water Purification. *J. Am. Chem. Soc*. 147 (**2025**) 43086-43097.

Electronic Supplementary Material

Rapid water purification enabled by balancing metal and non-metal electron transfer channel in peroxymonosulfate activation

Yuxuan Bai [1], Ganbing Zhang [2], Yetong Hua [1], Tiantian Hao [1], Zhaoyu Qiao [1], LiJuan Tian [1], Yi Shi [1], and Hui Xu [1]✉.

[1] *State Key Laboratory of Green Pesticide, Engineering Research Center of Photoenergy Utilization for Pollution Control and Carbon Reduction, Ministry of Education, College of Chemistry, Central China Normal University, Wuhan 430079, China*

[2] *Collaborative Innovation Center for Advanced Organic Chemical Materials Co-constructed by the Province and Ministry, Ministry-of-Education Key Laboratory for the Synthesis and Applications of Organic Functional Molecules, College of Chemistry and Chemical Engineering, Hubei University, Wuhan 430062, China*

Supplementary Text

Texts S1-S10.

Text S1 Chemicals and reagents

All reagents were commercially available and used without further purification. Cobalt chloride hexahydrate ($CoCl_2 \cdot 6H_2O$), ferrous chloride tetrahydrate ($FeCl_2.4H_2O$), cobaltosic oxide (Co_3O_4), cuprous chloride dihydrate ($CuCl_2 \cdot 2H_2O$), hexaaminobenzene (HAB) were purchased from Shanghai Macklin Biochemical Co., Ltd. Quenching agents of methanol (MeOH), tert-butanol (TBA), L-histidine (L-His)

and methyl phenyl sulfoxide (PMSO) were supplied by Shanghai Aladdin Biochemical Technology Co.,Ltd. PMS($2KHSO_5 \cdot KHSO_4 \cdot K_2SO_4$),

Deuterium oxide (D_2O), $NH_3.H_2O$, sodium bicarbonate ($NaHCO_3$), sodium dihydrogen phosphate dihydrate ($NaH_2PO_4 \bullet 2H_2O$), nitrate ($NaNO_3$), calcium chloride ($CaCl_2$), sodium chloride (NaCl), Potassium iodide (KI), humic acid (HA) were provided by Shanghai Bide Pharmaceutical Technology Co., Ltd. 2,4-dichlorophenol (2,4-DCP), Bisphenol A (BPA), phenol (PE), 4-nitrobenzoic acid (NBA), acetaminophen (APAP),

carbamazepine (CBZ), atrazine (ATZ), sodium thiosulfate ($Na_2S_2O_3$) were purchased

from Sinopharm Chemical Reagent Co., Ltd. 2,2,6,6-tetramethyl-4-piperidinone (TEMP), 5,5-dimethyl-pyrroline-N-oxide (DMPO), Deuterium oxide (D_2O), Nitrotetrazolium blue chloride (NBT), coumarin were purchased from Shanghai Yuanye Biotechnology Co., Ltd.

Text S2 Characterizations

The morphologies of samples were examined by transmission electron microscopy (TEM), using JEM-2100 (Japan) and FEI Talos F200x (Thermo Fisheries, USA) instrument, respectively. The aberration corrected high angle annular dark field scanning transmission electron microscopy (AC-HAADF STEM) images was obtained via Thermo Fisheries Titan Themis G2 60-300 with a spherical aberration corrector working at 300 kV. Field emission scanning electron microscope (FE-SEM) images were obtained via a JSM7900F (Japan) instrument. The structural information was obtained by Fourier transform spectrophotometer (FT-IR, TENSOR 27, Bruker, Germany). X-ray photoelectron spectroscopy (XPS) measurements was collected on Thermo Fisheries Escalab 250Xi (USA). All XPS spectra were corrected according to the C1s line at 284.6 eV. The ultraviolet-visible (UV-Vis) spectra were obtained via a Shimadzu 2401PC reader (Shimadzu, Japan). Photoluminescence (PL) spectra were recorded at room temperature on a fluorescence spectrophotometer (Edinburgh Instruments, FLS1000) under the excitation of a 375 nm light source. Electron paramagnetic resonance (EPR) spectra were conducted on a Bruker EMXPLUS instrument (Germany). Total organic carbon (TOC) was measured by a TOC analyzer (TOC-VCPH, Japan). The cobalt leaching rates and cobalt content of catalysts were conducted by inductively coupled plasma atomic emission spectroscopy. (ICP-MS, ICAP 7200, Thermo Fisher, USA).

Text S3 Catalytic performance evaluation

The degradation kinetics of the contaminants followed pseudo-first-order kinetics, with the reaction rate constants (k_{obs}) calculated using the following equation:

$$\ln\left(\frac{C_t}{C_0}\right) = -k_{obs} \times t \quad \text{(Eq. S1)}$$

where C_t is the concentration of the contaminant at time t, and C_0 is the initial concentration at time t_0.

$$\text{k-value}= \frac{\text{ln}(C_0/C_t)}{c[\text{Catalyst}]*c[\text{PMS}]} \quad \text{(Eq. S2)}$$

The modified kinetic rate constant (k-value) for the degradation of pollutant was determined by normalizing the observed rate constant to the catalyst dosage and PMS (oxidizing agent) concentration, and subsequently scaling it with the concentration of pollutant.

Text S4 $SO_4^{\cdot-}$ concentration measurements

The p-hydroxybenzoic acid (p-HBA) is used as $SO_4^{\bullet-}$ probe molecule as 1 mole $SO_4^{\bullet-}$ can react with 1 mol p-HBA to generate 1 mol p-benzoquinone (p-BQ). Therefore the generated p-BQ concentration was quantified by HPLC with the mobile phase is Acetonitrile/0.1% formic acid (40/60, v: v) and the detection wavelength is 246 nm.

Text S5 Details of NBT probe experiment

NBT was used as a probe to detect the generation of $O_2^{\cdot-}$ during the catalytic reaction [1]. Specifically, 5 mg of catalyst was dispersed in 50 mL of 0.05 mM NBT solution. After stirring for 10 min, 1 mL of the solution was sampled as the initial reference. Post the addition of PMS, 1 mL aliquots were taken at set intervals, immediately filtered through a 0.22 μm membrane, and the absorbance was measured at 259 nm using a UV-visible spectrophotometer.

Text S6 Contribution of $SO_4^{\bullet-}$ and ETP on 2,4-DCP removal in the M-HAB/PMS systems

The contribution of ROS to 2,4-DCP oxidation in the Co-HAB/PMS, Fe-HAB/PMS and Cu-HAB/PMS system was determined according to the literature as follows.

$$\lambda(SO_4^{\bullet-}) = [(k_0–k_1)/k_0] \times 100\% \quad \text{(Eq. S3)}$$

$$\lambda(\text{ETP}) = 1-\lambda(\text{radicals}) \quad \text{(Eq. S4)}$$

Where k_0 is the reaction rate constant without quenching agent, and k_1 is the reaction rate constants with the addition of MeOH.

Text S7 Fabrication of M-HAB/PVDF composite catalytic membrane

The M-HAB (M=Fe, Co, Cu) catalyst (10 mg) was dispersed in aqueous solution and subjected to ultrasonic treatment for 30 min. Subsequently, the M-HAB catalyst was deposited on a PVDF membrane (pore size=0.2 μm) via a direct vacuum-assisted filtration of M-HAB suspensions.

Text S8 In situ Raman analysis

In situ Raman spectroscopy observation was determined by a confocal microscopic Raman spectrometer (LABRAM HR EVO, Horiba Co., Japan) with a 532 nm excitation wavelength. For analysis, the M-HAB catalyst was formed into discs with approximately 1.0 mm thickness and 12.6 mm in diameter. Drops of 200 μM PMS solution were applied to these discs. The Raman spectra were then collected over a range of 700.0 to 1700.0 cm^{-1} at a resolution of 1.0 cm^{-1}.

Text S9 DFT Calculations

Cluster model and density functional theory (DFT) method have been used to characterize the structures, properties, and mechanisms in the present system. In the calculations, clusters C36H36M5N20 (M=Fe, Co, and Cu) were constructed for modeling the coordination environment of the MOFs (Metal-Organic Frameworks) with the three metals, the spin-unrestricted DFT calculation with wB97XD functional [2] which includes long-range correction and the Grimme's D2 dispersion correction term, and the basis set of Stuttgart/Dresden Dubble-zeta basis set (SDD) [3]along with relativistic effective core potential for transition metals (Fe, Co, and Cu) and 6-311G(d,p) for the other nonmetal were used to optimize the geometries of the catalyst clusters, PMS adsorbed clusters, and various evolution species corresponding to minimum total energies. The frequency calculation was used to verify the optimized geometry corresponds to the energy minimum, and obtained the thermodynamic functions. Based on the optimal geometries, energies for all species were calculated by wB97XD functional and the basis set of SDD for Fe, Co, and Cu, and 6-311++G(2d,p) for the other nonmetal. Natural population analysis (NPA) was carried out for calculating the natural charges. All these calculations were carried out

by Gaussian 16 program [4]. The Multiwfn 3.8 program [5-6] was used to calculate partial density of states (PDOS) of Fe, N, O, d-band center of Fe, electron localization function (ELF) and core-valence bifurcation (CVB) index [7], visualize the geometric structures, molecular orbitals, and ELF. The adsorption energy (E_{ads}) of PMS at central metal sites of the catalyst clusters were calculated according to the following formula.

$$E_{ads}=E_{total}-E_{catal}-E_{PMS} \text{ (Eq. S5)}$$

Where E_{total} stands for the total energy of the adsorbed species, E_{catal} and E_{PMS} represent the energy of the catalyst cluster surface and the free PMS molecule, respectively.

Text S10 Electrochemical measurements

Electrochemical experiments, including timed open circuit potentials (OCPt), electrochemical impedance spectroscopy (EIS) and chronoamperometry (i-t), were conducted using a CHI760E electrochemical workstation (Shanghai Chenhua Apparatus Corporation, China). In a typical three-electrode system in a 50 mM Na_2SO_4 electrolyte solution was employed. The system comprised a saturated Ag/AgCl reference electrode, a platinum wire counter electrode, and a glassy carbon electrode coated with the catalyst as the working electrode. To prepare the working electrode, a catalyst ink was prepared by ultrasonically blending 10 mg catalyst with 50 μL of a 5.0 wt.% Nafion dispersion and 950 μL of water and ethanol. Subsequently, 100.0 μL of this ink was carefully dropped onto the surface of a freshly the FTO glass electrode and allowed to dry at room temperature. Chronoamperometry was conducted at open-circuit potential. To explore interactions between the catalyst, oxidant, and contaminant, PMS and 2,4-DCP were sequentially added to the electrolyte in different sequences at specified intervals for measurement. EIS was measured with a three-electrode system in 1 M KCl solution containing 5 mM K_3[Fe $(CN)_6$]/K_4[Fe $(CN)_6$] (1:1) mixture as the electrolyte in a frequency range of 0.1 Hz-100 kHz.

Figures S1-S43.

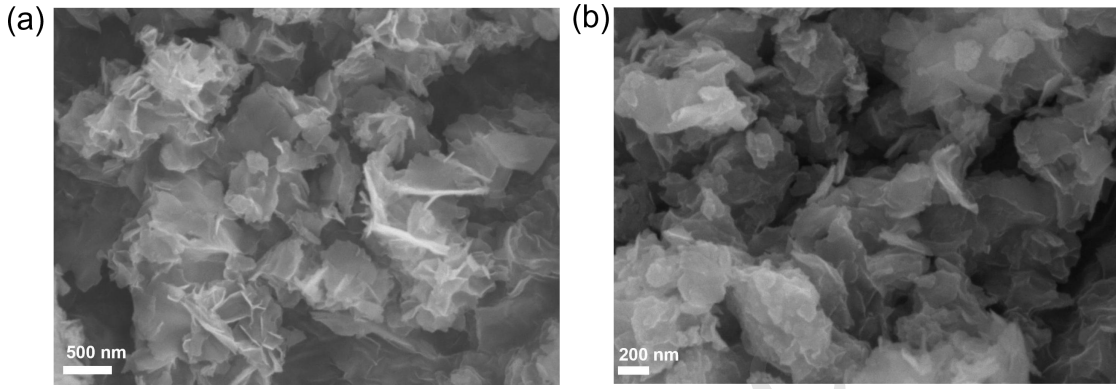

Figure S1. SEM images of Co-HAB.

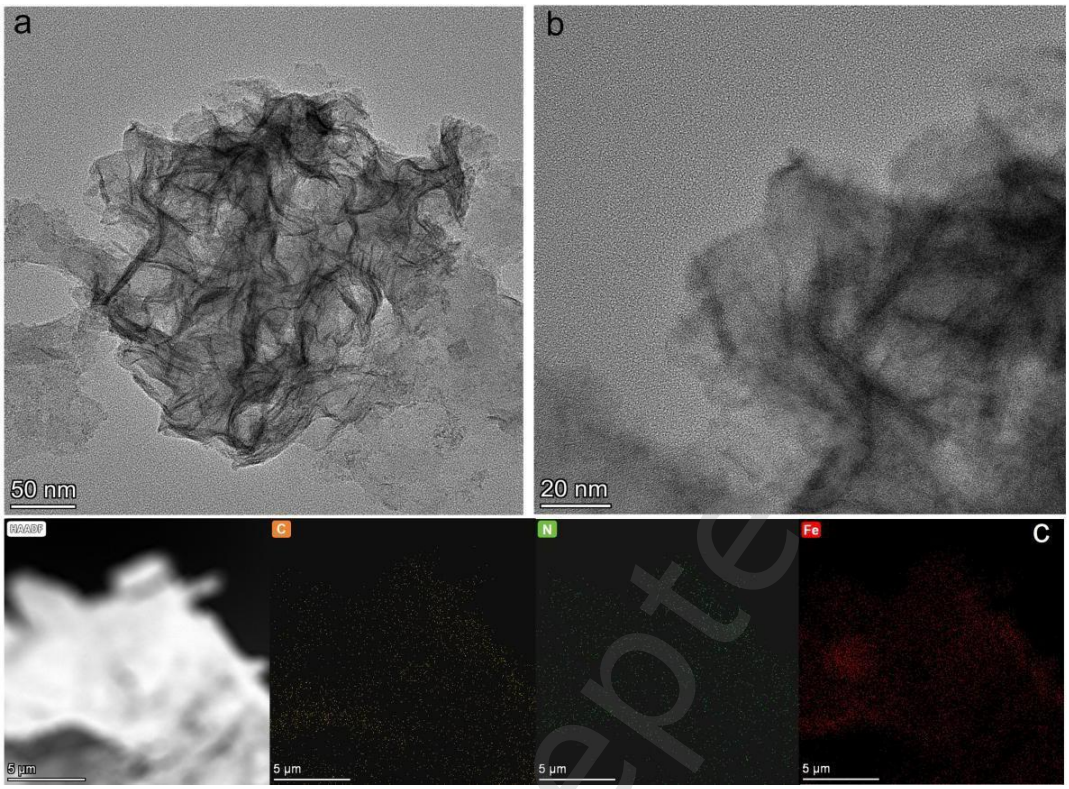

Figure S2. Morphology characterization of Fe-HAB. (a, b) STEM images of Fe-HAB, and (c) EDS mapping.

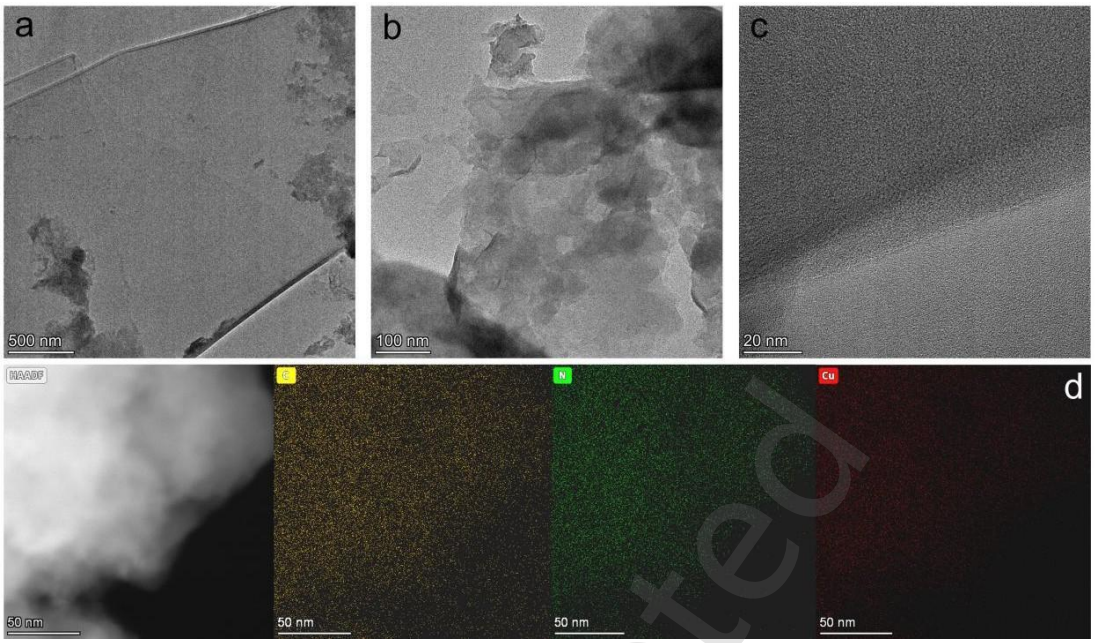

Figure S3. Morphology characterization of Cu-HAB. (a-c) STEM images of Cu-HAB, and (d) EDS mapping in 50 nm.

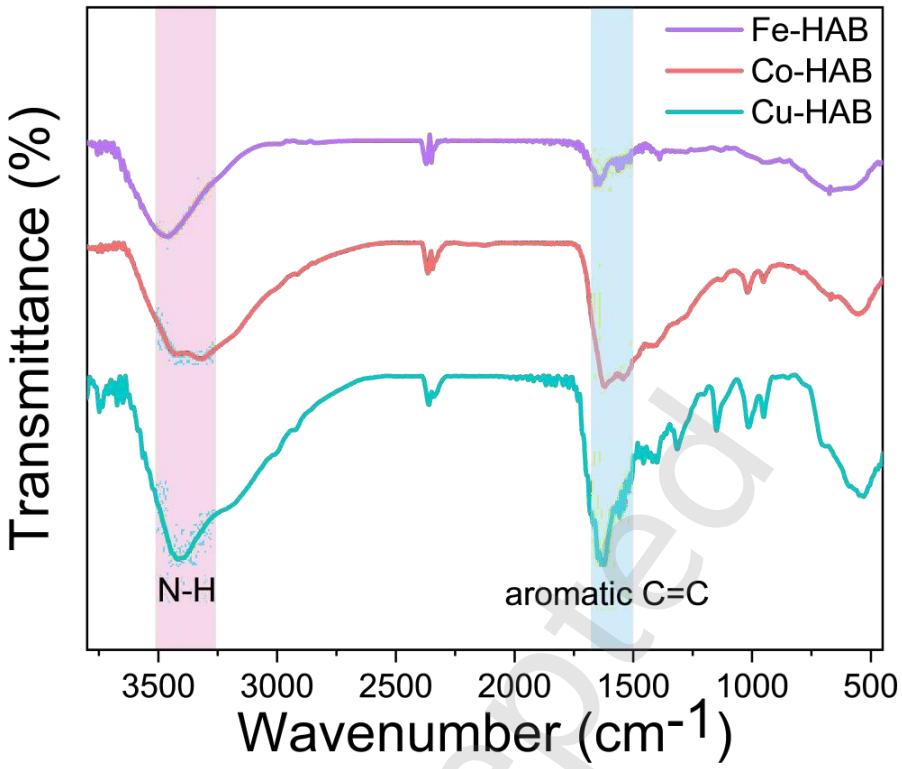

Figure S4. FTIR spectra of Fe-HAB, Co-HAB and Cu-HAB.

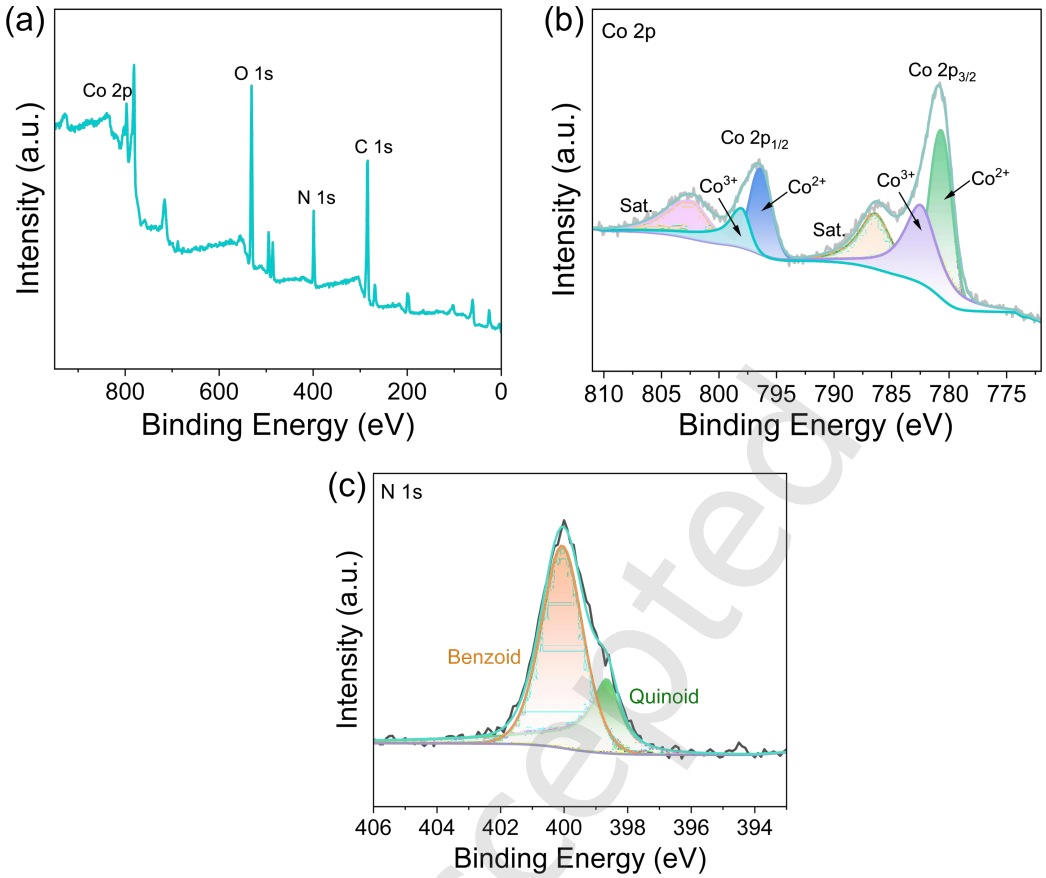

Figure S5. XPS analysis of Co-HAB. (a) Full energy spectrum for all the elements, (b) zoomed-in spectrum of Co 2p and (c) the N 1s energy region.

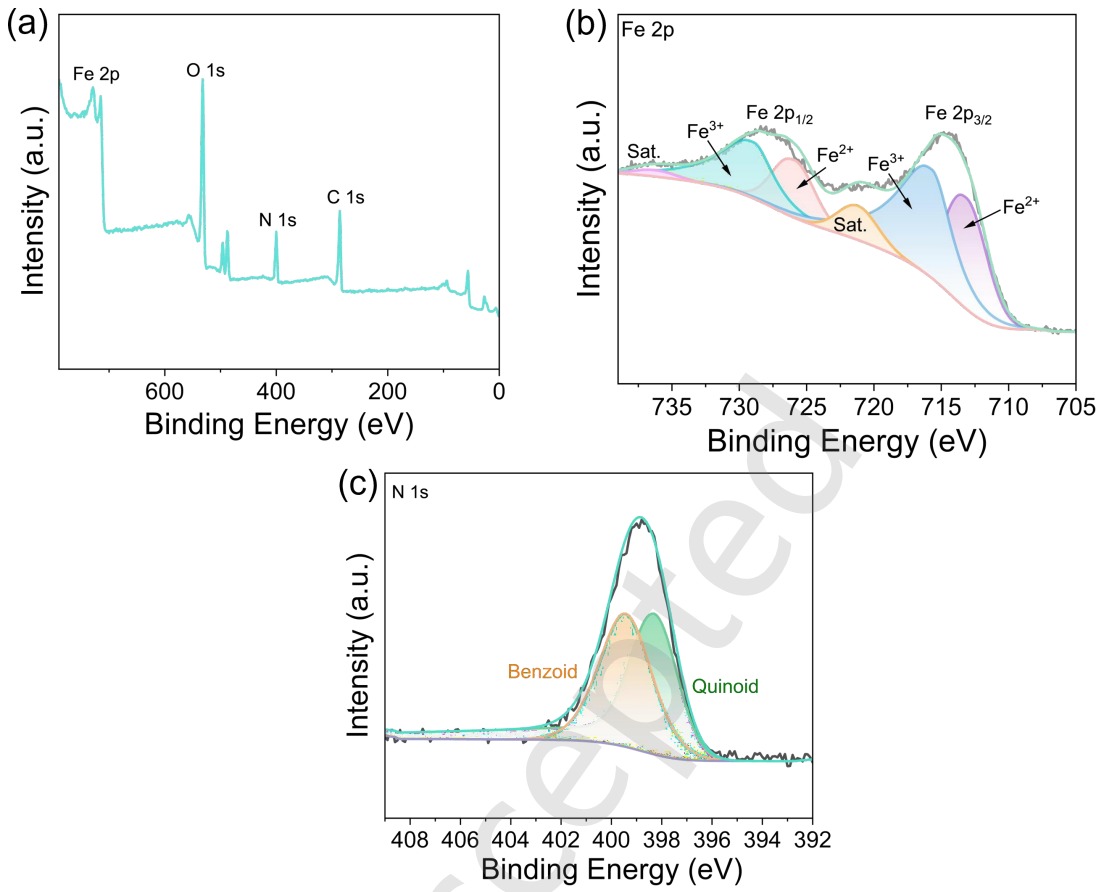

Figure S6. XPS analysis of Fe-HAB. (a) Full energy spectrum for all the elements, (b) zoomed-in spectrum of Fe 2p and (c) the N 1s energy region.

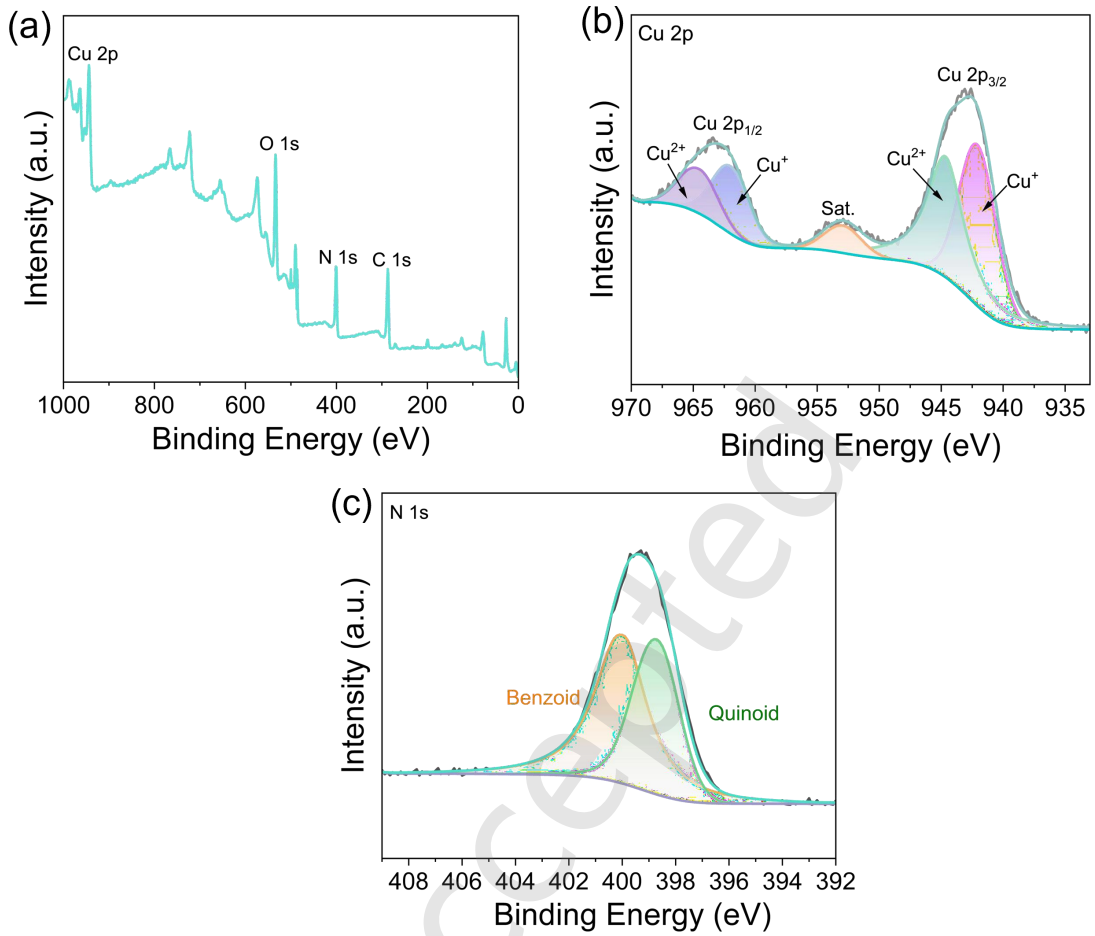

Figure S7. XPS analysis of Cu-HAB. (a) Full energy spectrum for all the elements, (b) zoomed-in spectrum of Cu 2p and (c) the N 1s energy region.

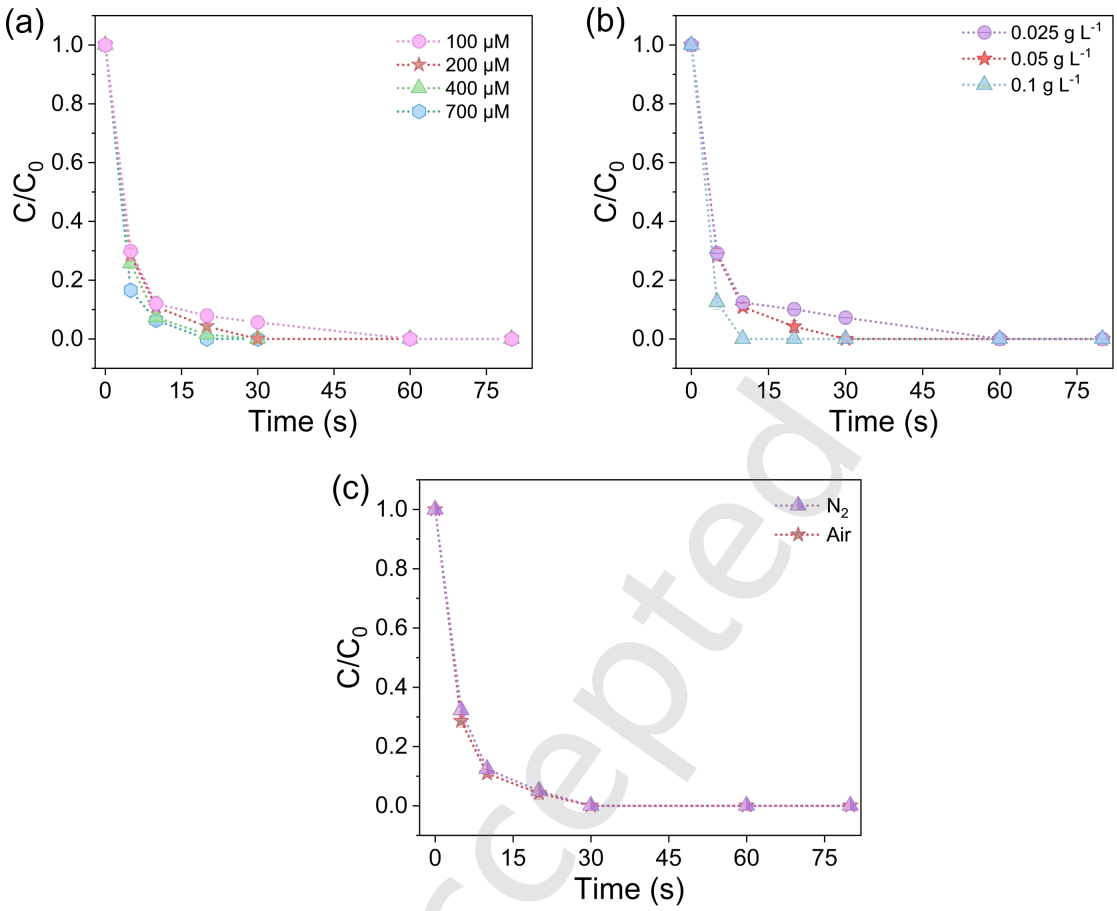

Figure S8. (a) Influence of PMS dosage, (b) Influence of catalyst dosage on the degradation kinetics of 2,4-DCP in Co-HAB/PMS system, (c) 2,4-DCP removal under different conditions.

Note: The removal rates of 2,4-DCP in both air and N_2-saturated systems showed no significant differences. These results indicate that O_2 does not contribute to the removal of 2,4-DCP.

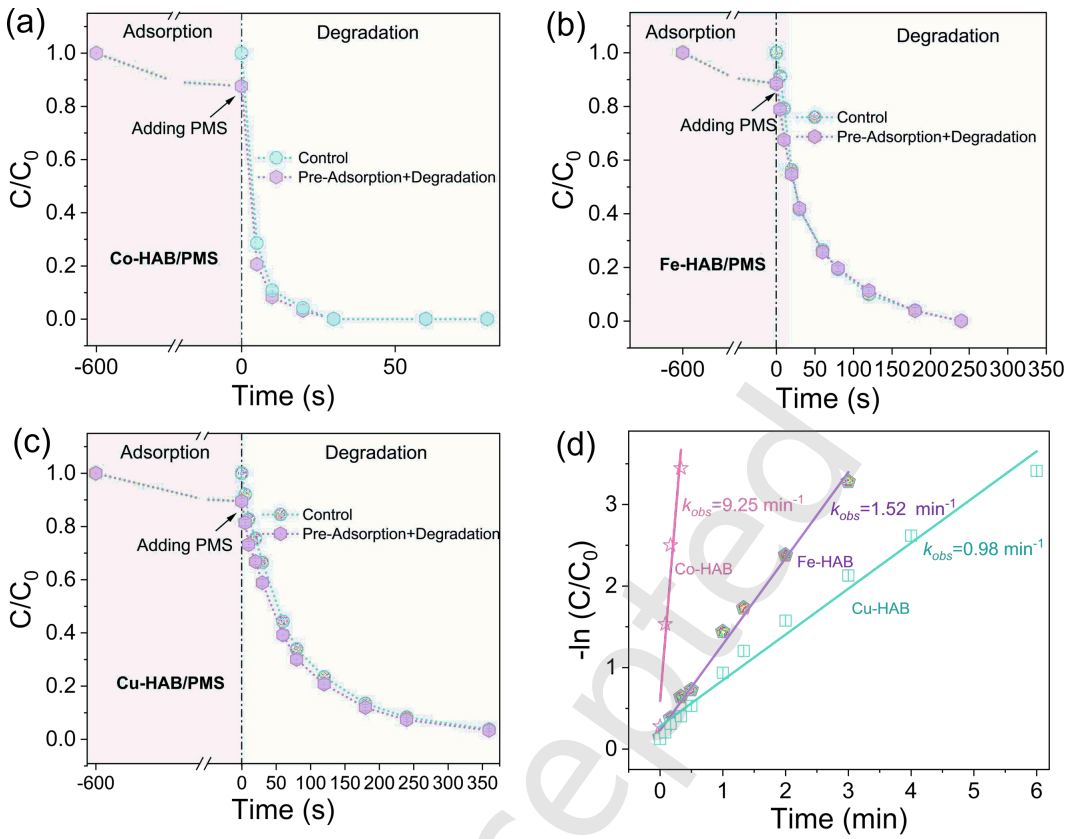

Figure S9. (a-c) Comparison of catalytic performance of pre-adsorption degradation and direct degradation in different systems; (d) Reaction kinetics of different systems. Reaction condition: $[2,4\text{-DCP}]_0$ = 10 mg L^{-1}, $[PMS]_0$=0.2 mM, [catalyst]=0.05 g L^{-1}, initial pH=7.0.

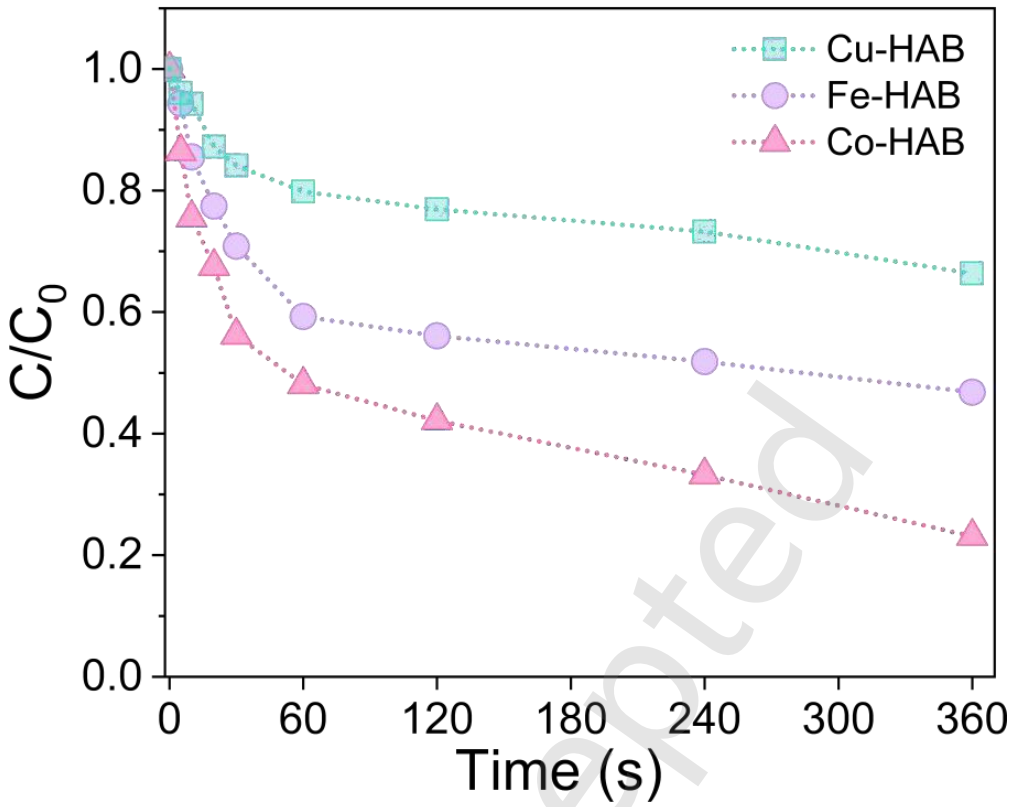

Figure S10. PMS decomposition in these different catalysts/PMS systems.

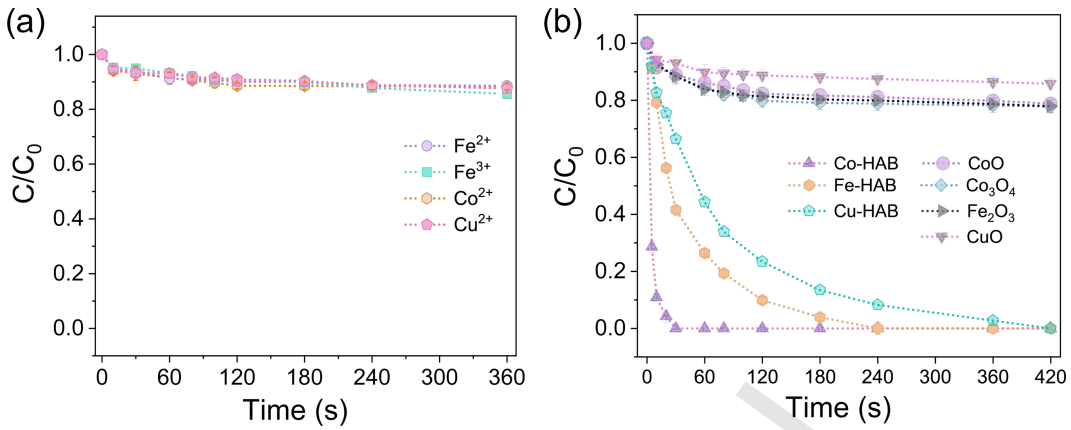

Figure S11. (a) 2,4-DCP degradation by Fe^{2+}, Fe^{3+}, Co^{2+}, and Cu^{2+} activated PMS systems; (b) The effects of heterogeneous catalysts Co_3O_4, CoO, Fe_2O_3, and CuO on the degradation of 2,4-DCP. (The error bars are all standard deviations calculated from the results of three parallel experiments).

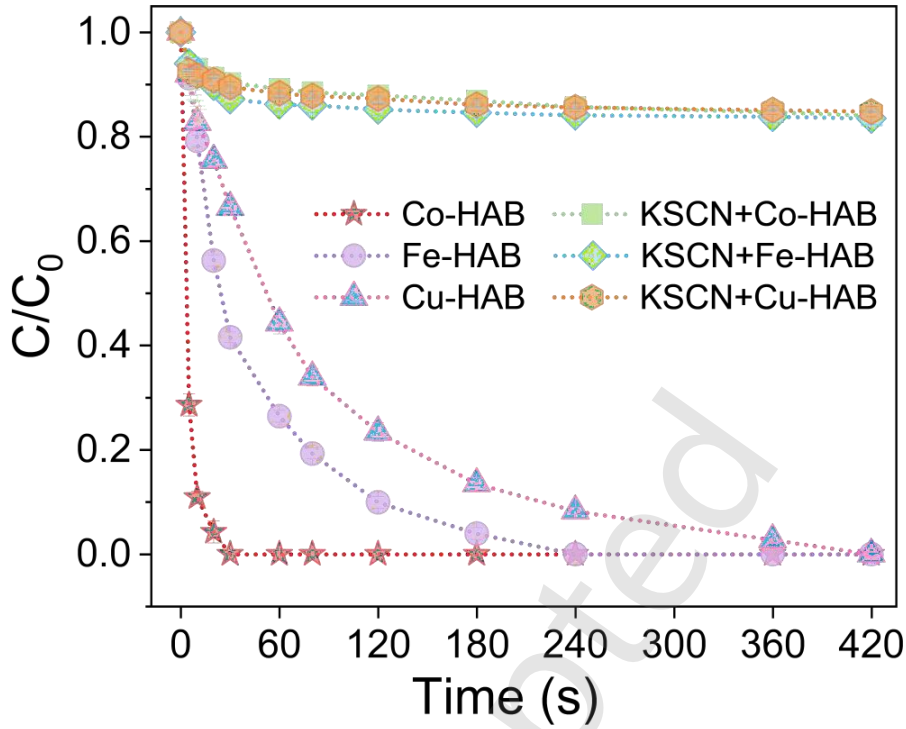

Figure S12. Time profiles of 2,4-DCP degradation in Co-HAB/PMS, Fe-HAB/PMS and Cu-HAB/PMS systems with KSCN. Reaction condition: [2,4-DCP] =10 mg L^{-1}, [PMS] = 0.2 mM, [catalyst] = 0.05 g L^{-1}, initial pH = 7.0.

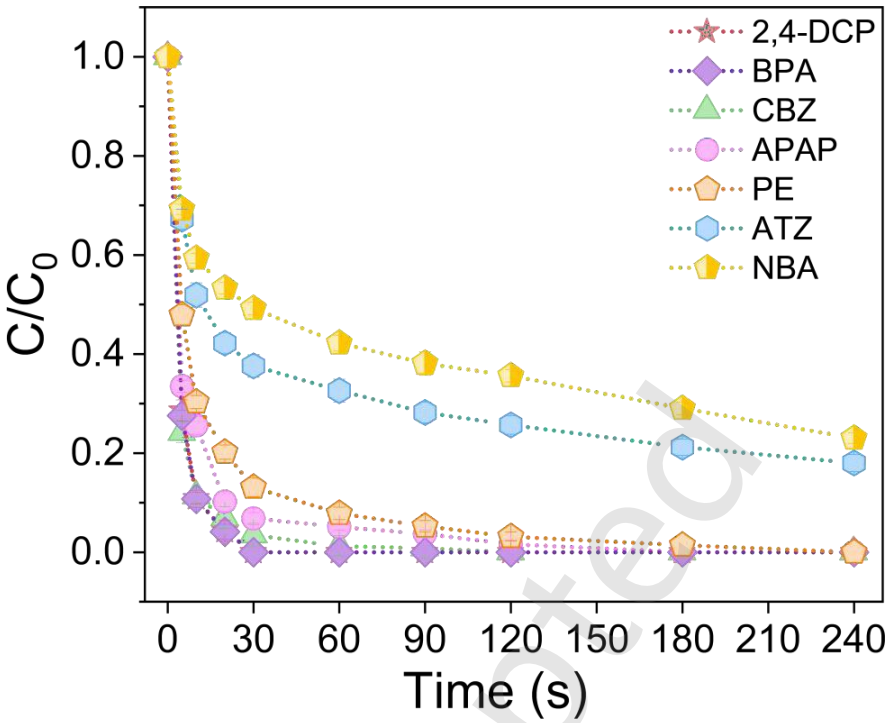

Figure S13. Degradation of various organic pollutants in the Co-HAB/PMS system.

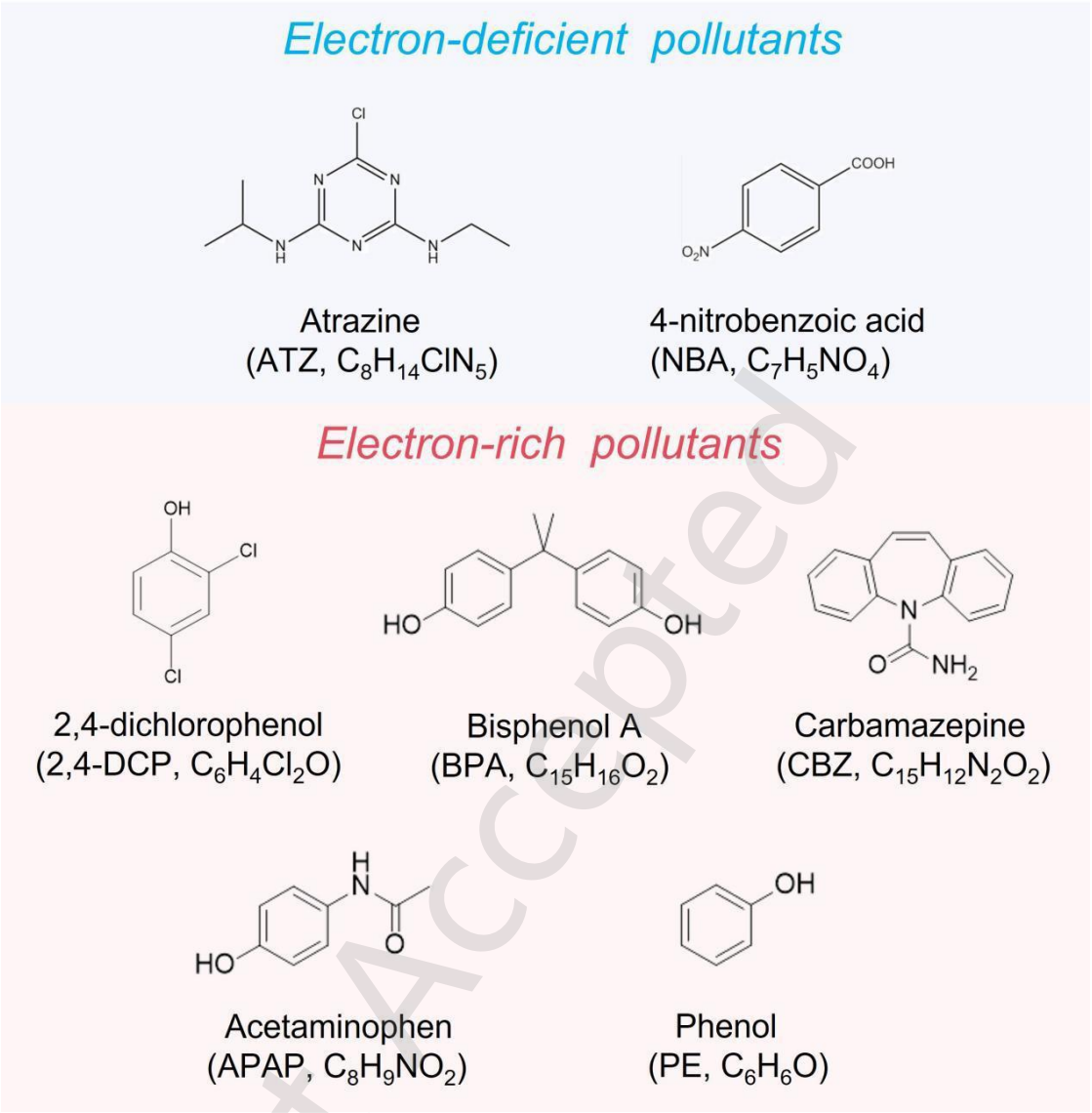

Figure S14. The chemical structures of various refractory pollutants.

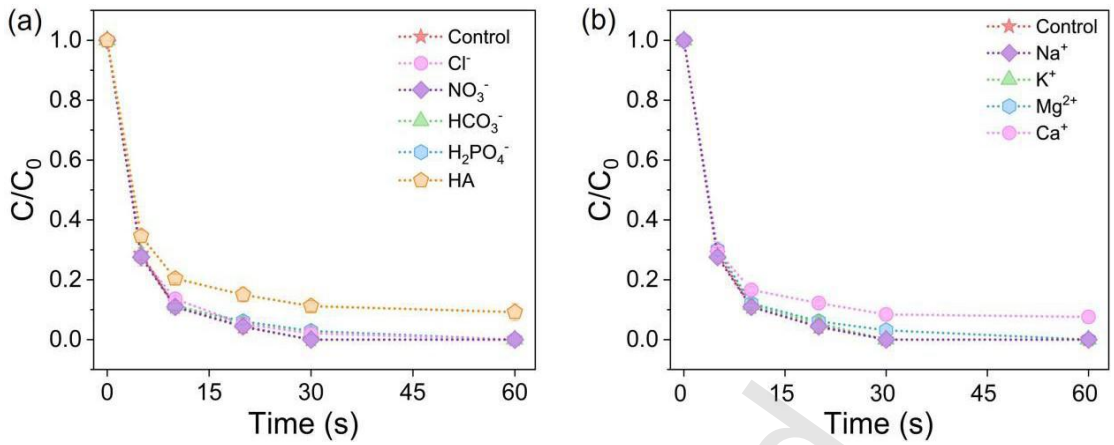

Figure S15. Co-HAB/PMS catalytic degradation rate with interference of 0.2 M salts and humic acid.

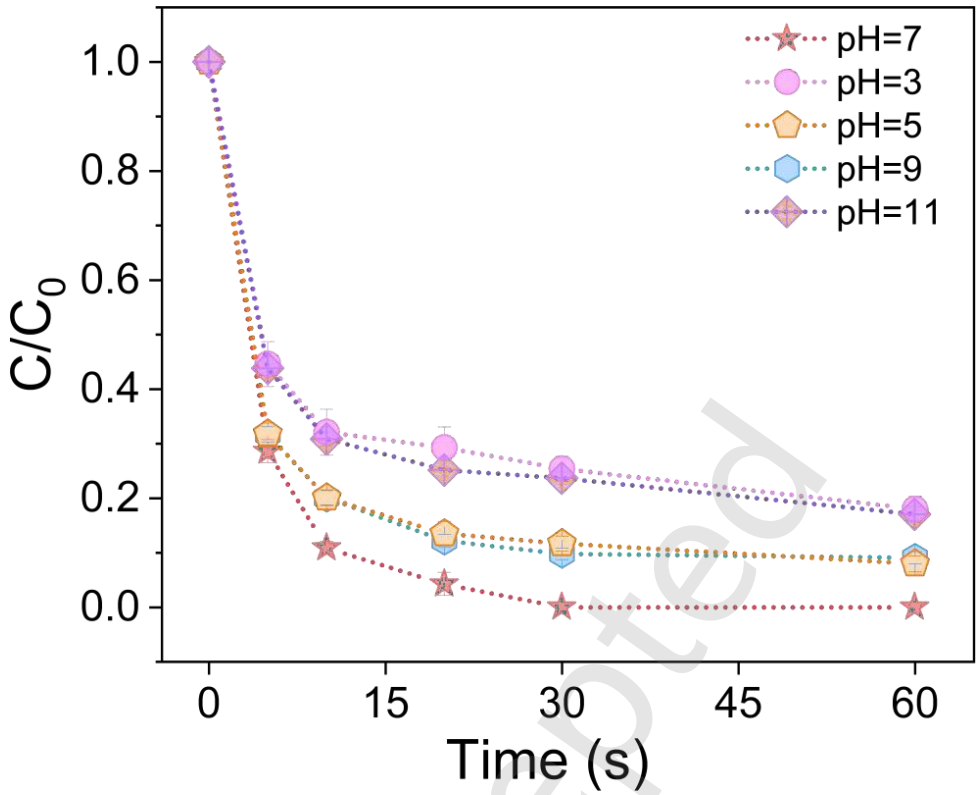

Figure S16. The effect of reaction pH on 2,4-DCP removal.

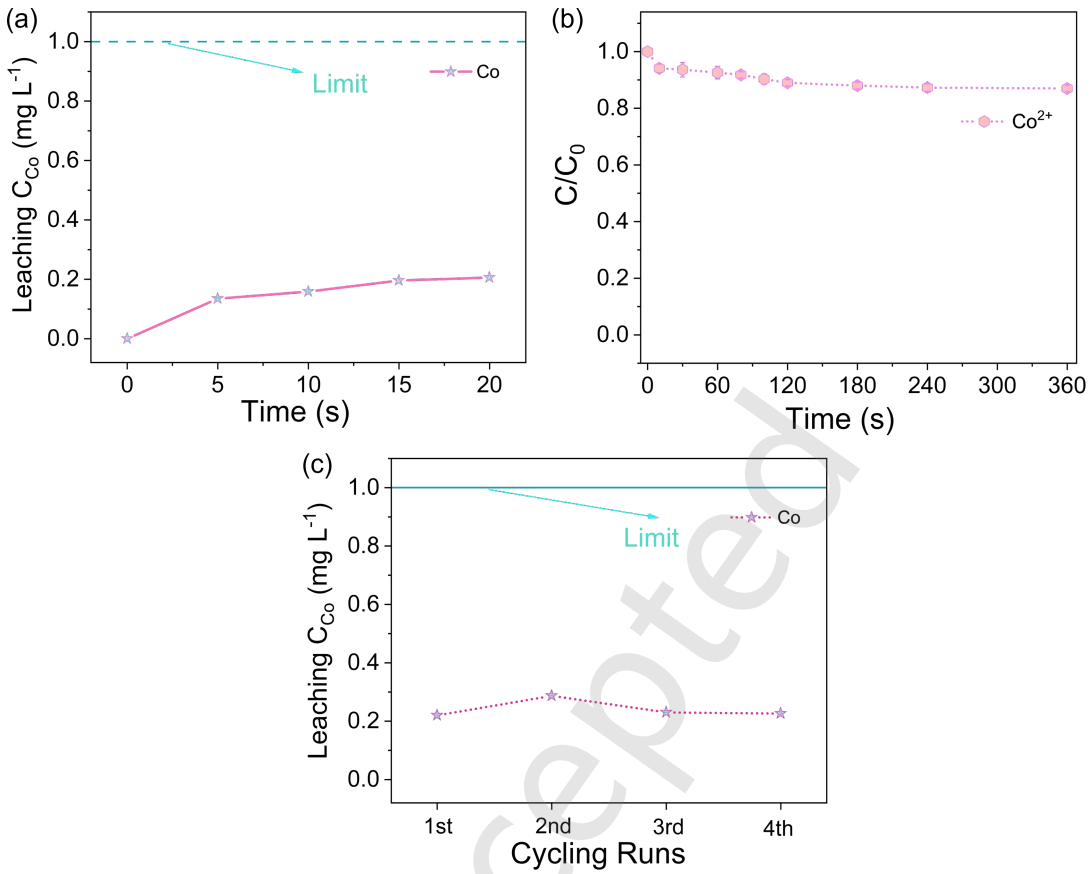

Figure S17. (a) The acceptable limit standard of Co in the surface water environment and the Co leaching during 2,4-DCP removal process in Co-HAB/PMS system; (b) Effect of leached Co ions on the degradation of 2,4-DCP; (c) Leaching concentration of Co ions after four cycles.

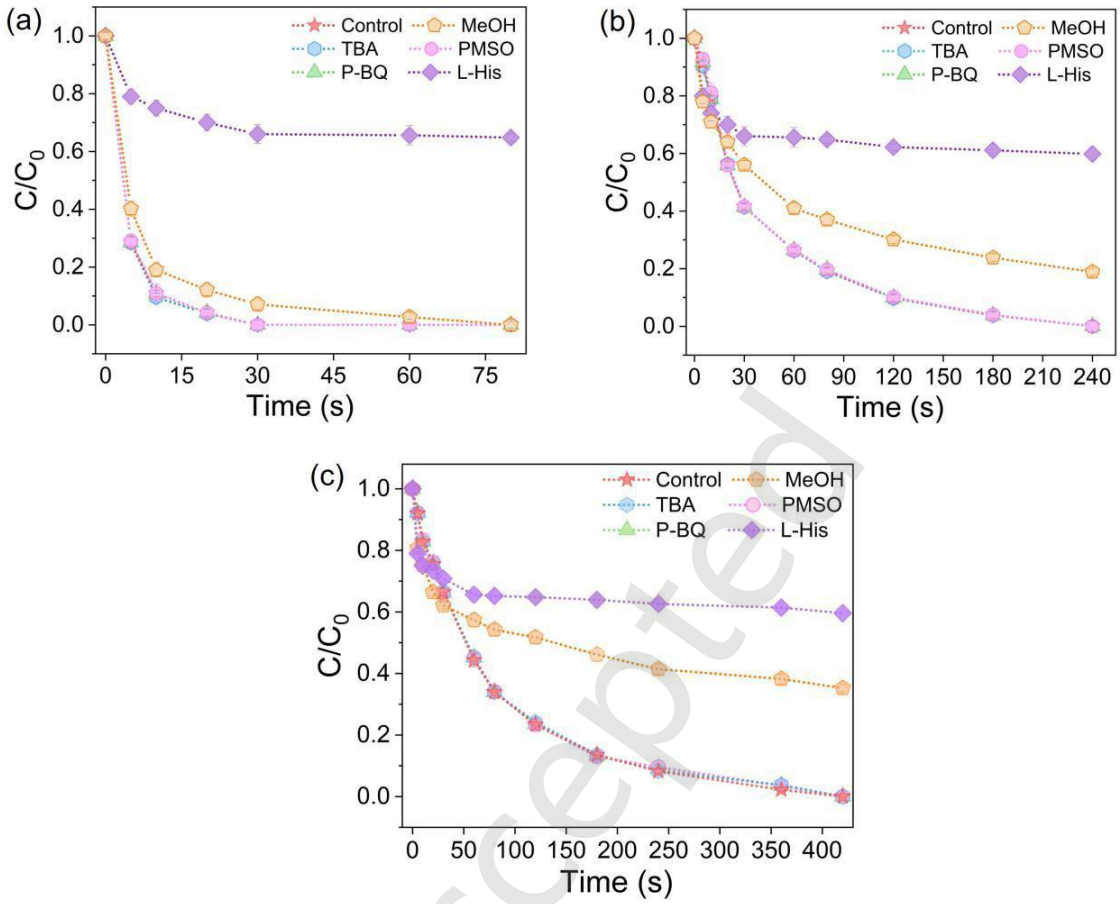

Figure S18. Investigation of active species in the 2,4-DCP system. (a) Degradation of 2,4-DCP in (a) Co-HAB/PMS system with different quencher; (b) Fe-HAB/PMS system and (c) Cu-HAB/PMS system.

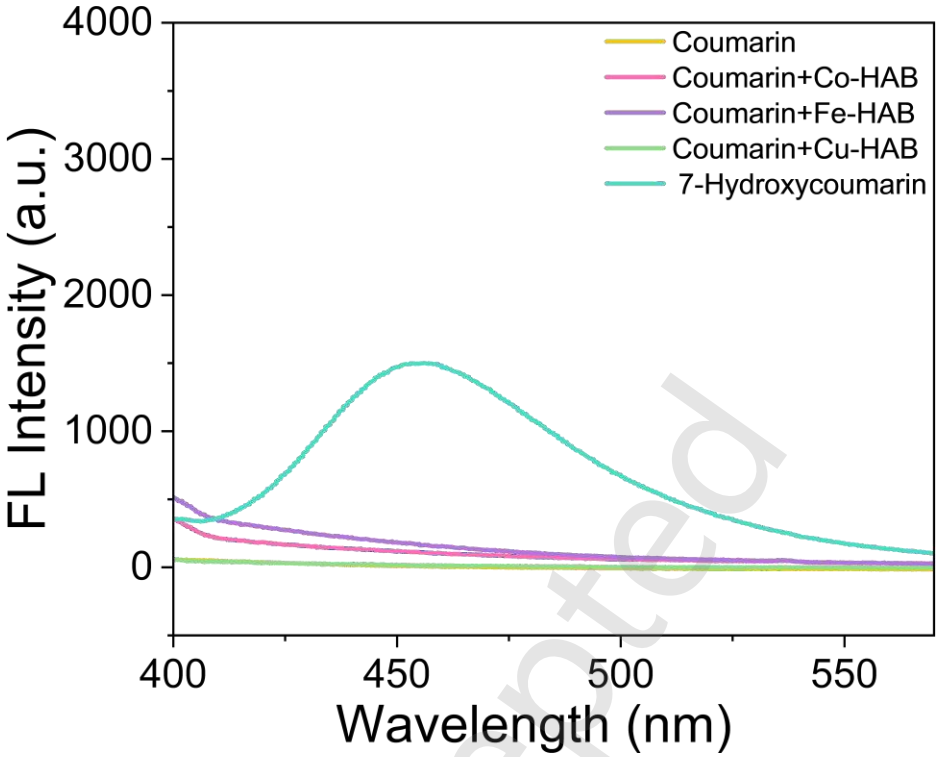

Figure S19. Fluorescence spectra of a catalytic system reacting with coumarin.

Note: Coumarin (the probe for •OH) was converted into 7-hydroxycoumarin during the reaction and exhibits a weak blue fluorescence emission at 460 nm at 350 nm excitation.

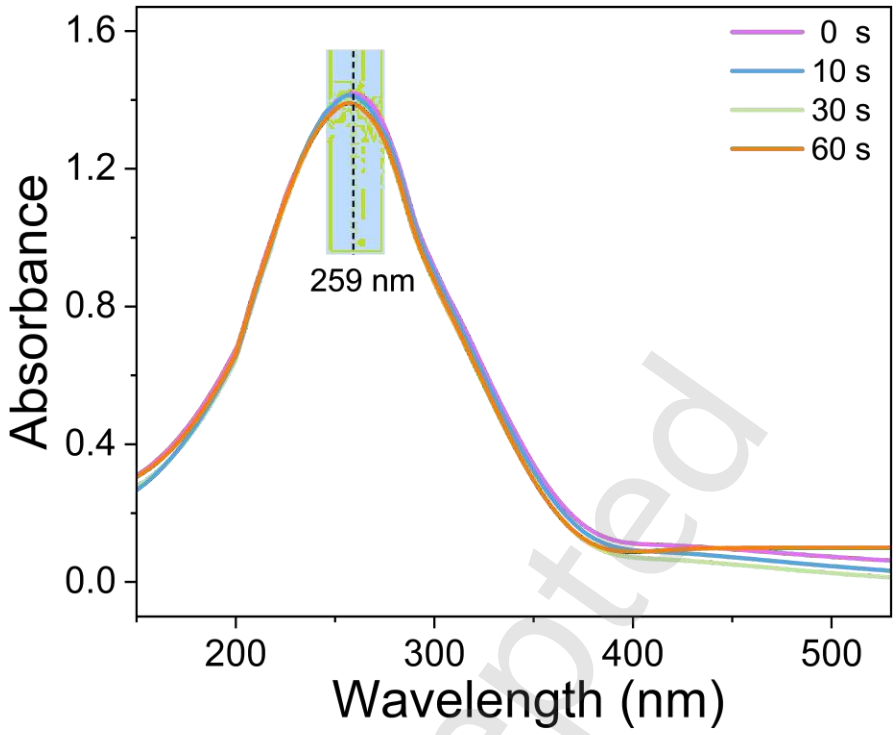

Figure S20. UV spectra of NBT transformation for determining $O_2^{\cdot-}$ in the Co-HAB/PMS system.

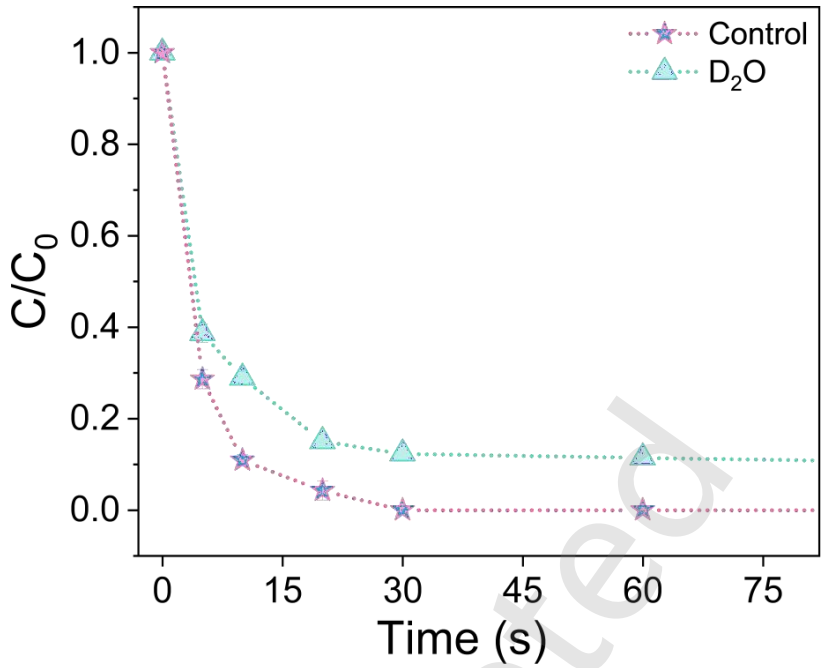

Figure S21. Comparative experiment of substituting H_2O with D_2O in Co-HAB/PMS system.

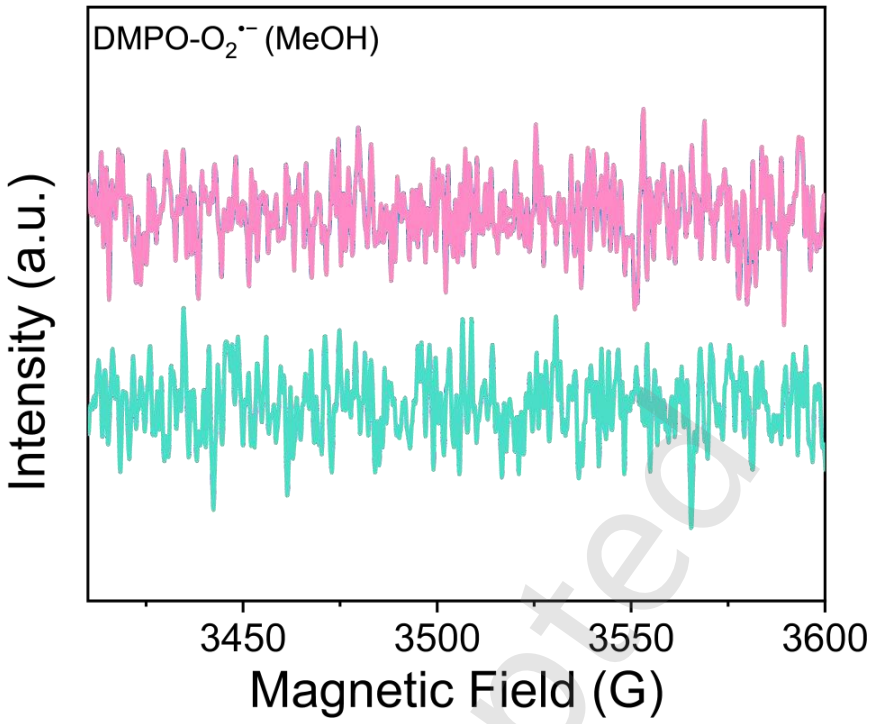

Figure S22. The EPR spectra in Co-HAB/PMS systems.

Note: $O_2^{\bullet-}$ was identified with DMPO (200 mM) as the spin-trapping agent in the methanol media.

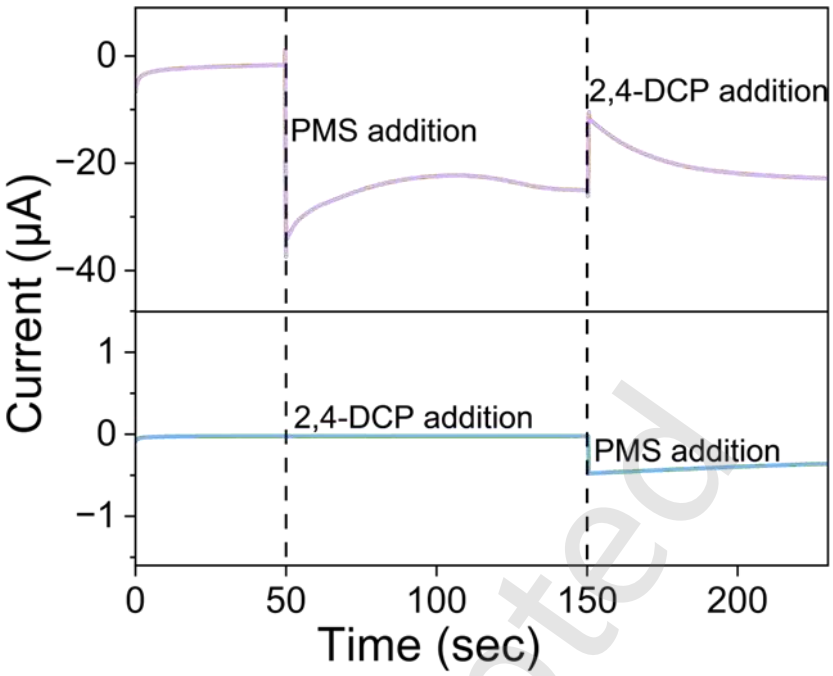

Figure S23. Chronoamperometry (i−t) profiles**.**

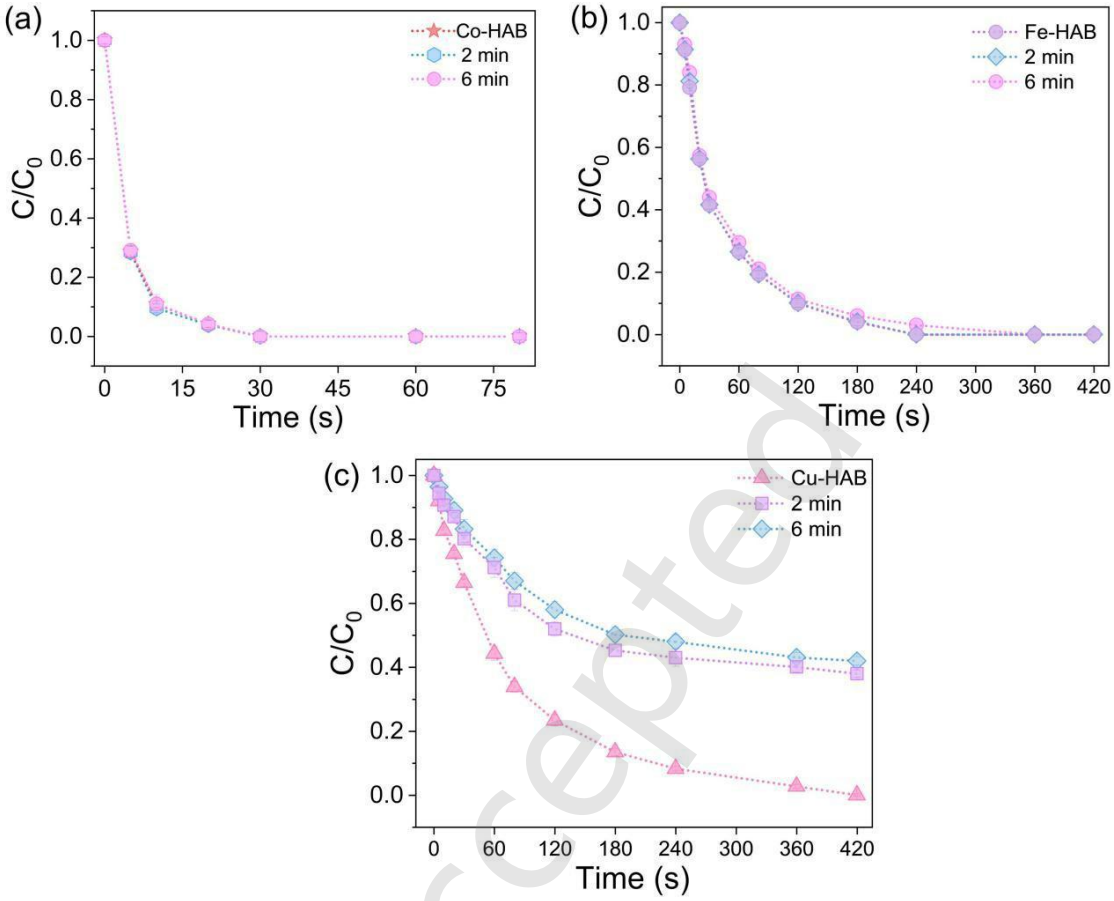

Figure S24. The removal efficiency of 2,4-DCP after mixing PMS and (a) Co-HAB; (b) Fe-HAB and (c) Cu-HAB.

Note: Pre-mixing experiments, Co-HAB, Fe-HAB, and Cu-HAB were mixed with PMS for durations of 2 minutes and 6 minutes prior to 2,4-DCP addition. The results demonstrated that as the pre-mixing time increased, the inhibition on 2,4-DCP degradation in Co-HAB and Fe-HAB remained minimal, indicating that the influence of ETP on pollutant oxidation overwhelmed that of $SO_4^{\bullet-}$. Conversely, the degradation of 2,4-DCP in Cu-HAB showed a noticeable decay effect with the kobs values decreasing more than 60% after 6 minutes of premixing. During the premixing of Cu-HAB with PMS, $SO_4^{\bullet-}$ were continuously consumed, resulting in a substantial reduction in the density of $SO_4^{\bullet-}$ available for degradation reactions. Since $SO_4^{\bullet-}$ were continuously consumed during the premixture of Cu-HAB and PMS, the density of

$SO_4^{\bullet-}$ available for degradation reactions was greatly reduced. This finding supports the hypothesis that PMS decomposes to generate $SO_4^{\bullet-}$ in the absence of 2,4-DCP.

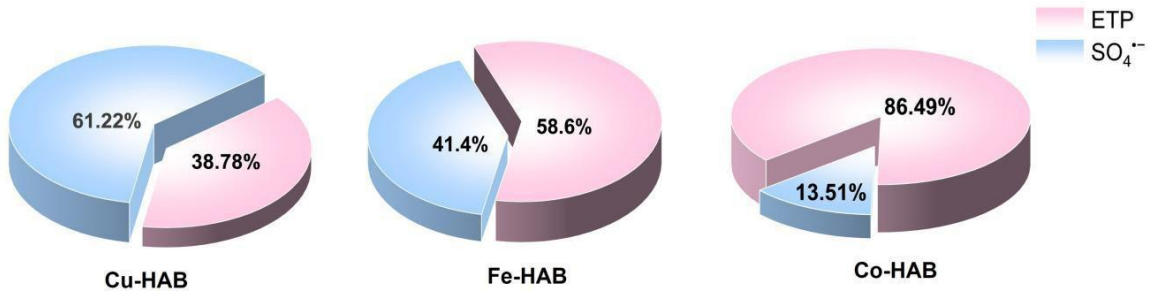

Figure S25. Proportion of active species in M-HAB/PMS system.

Note: The results indicate that the ETP oxidation mechanism in Co-HAB accounts for as much as 86.49% of the overall contribution, while $SO_4^{\bullet-}$ contribute a lesser extent of only 9.25%, demonstrating that ETP serves as the predominant oxidation mechanism. In Fe-HAB, ETP maintains a slight dominance with a contribution ratio of 58.56%. In contrast, Cu-HAB exhibits a different behavior, with $SO_4^{\bullet-}$ contributing 61.22%, indicating that radical oxidation plays a dominant role in the degradation of 2,4-DCP within this system. Consistent with the previously mentioned catalytic oxidation performance ranking of Co-HAB > Fe-HAB > Cu-HAB, our findings suggest that the modulation of the central metal species selectively and effectively activates PMS, facilitating the formation of key PMS* intermediates at the metal sites. This effectively enhances the redox capacity of the catalyst and leads to a shift in the active species from sulfate radicals to the ETP oxidation pathway.

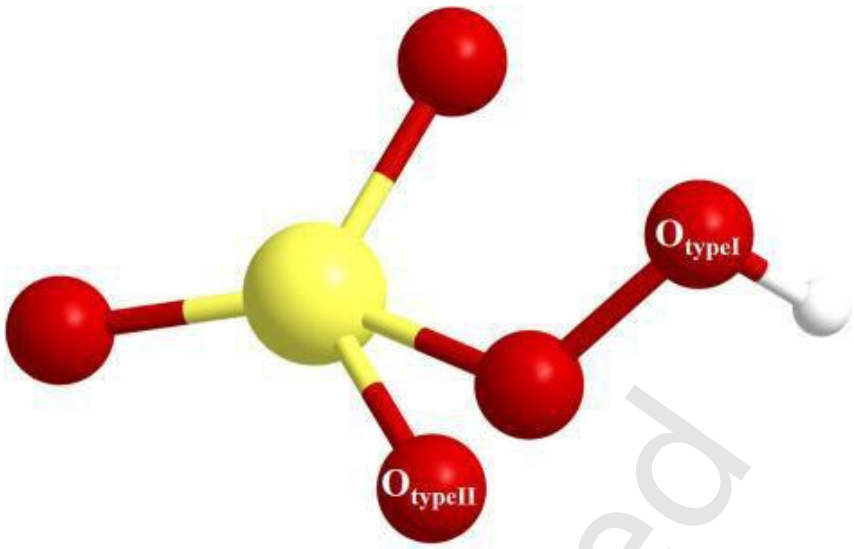

Figure S26. Molecular structure of PMS and the serial number of partial oxygen atoms. The yellow, red and white balls represented S, O and H, respectively.

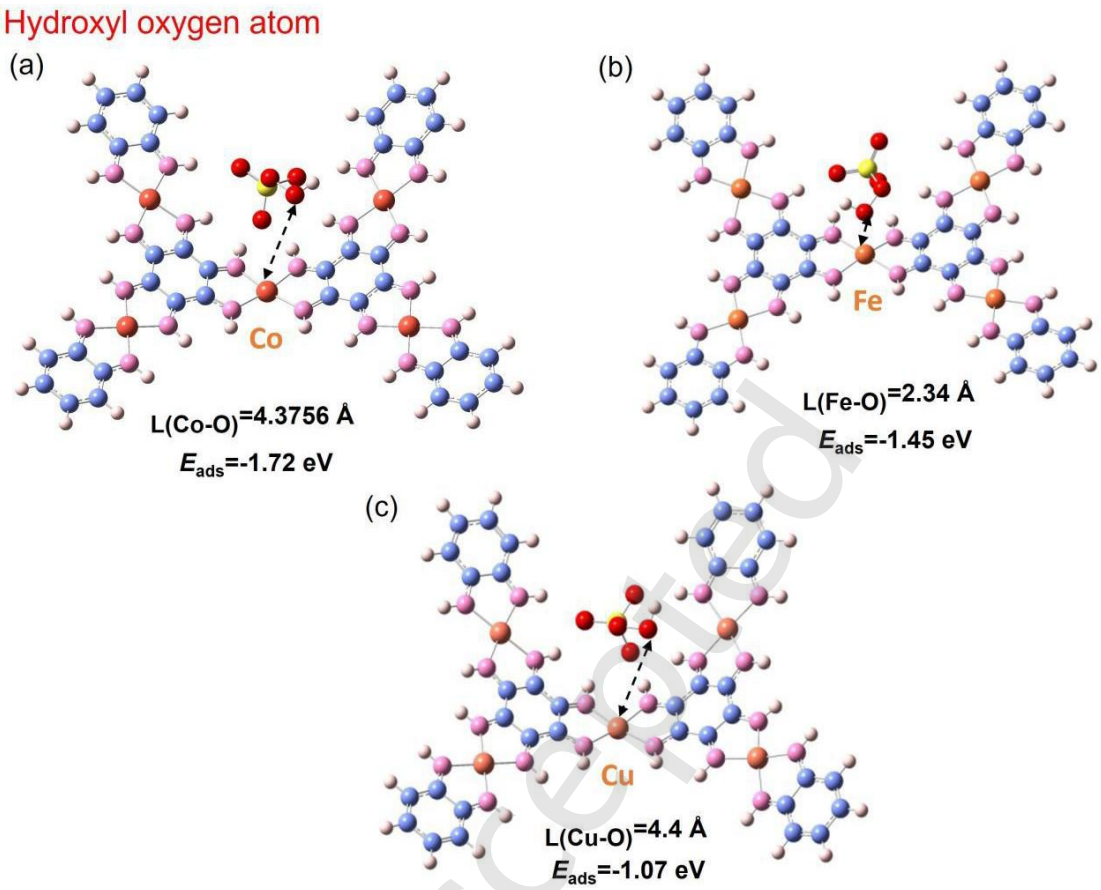

Figure S27. The adsorption model of the hydroxyl oxygen atom (O_{typeI}) and the bond lengths of (a) Co-HAB, (b) Fe-HAB and (c) Cu-HAB.

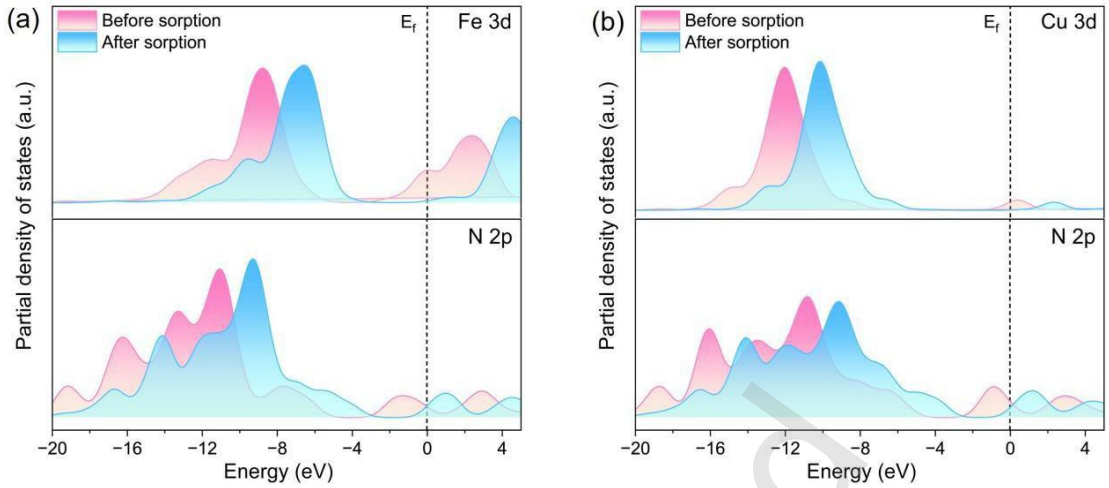

Figure S28. PDOS of (a) Fe 3d and N 2p and (b) Cu 3d and N 2p before and after PMS adsorption.

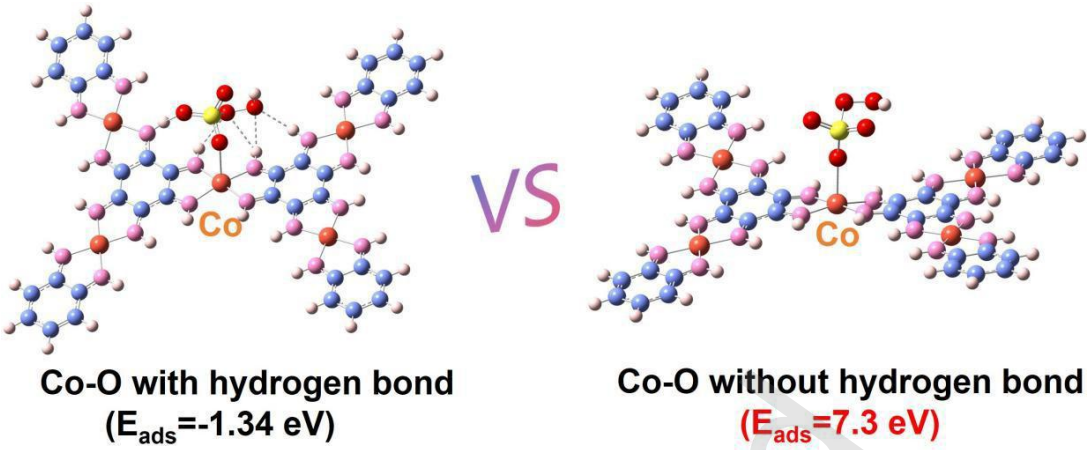

Figure S29. Influence of hydrogen bond on adsorption energy between Co-HAB and PMS.

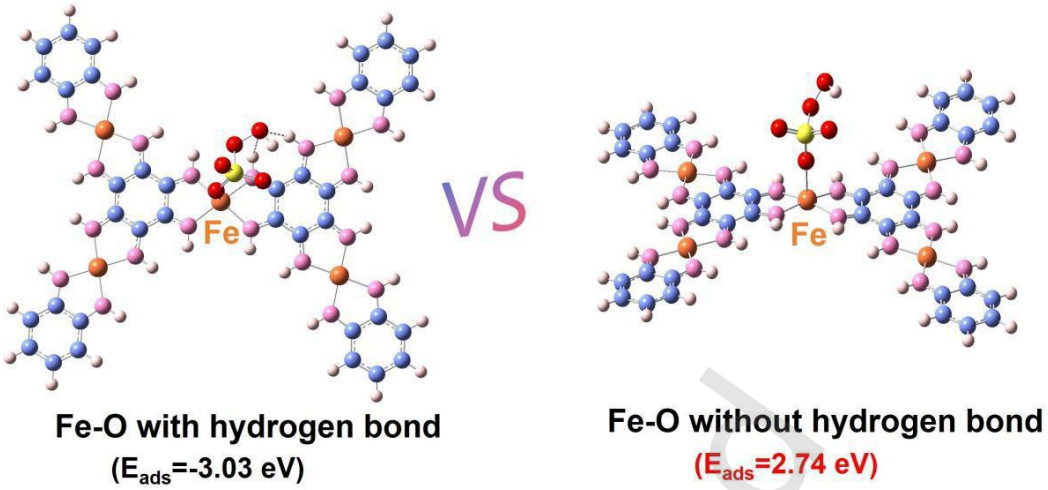

Figure S30. Influence of hydrogen bond on adsorption energy between Fe-HAB and PMS.

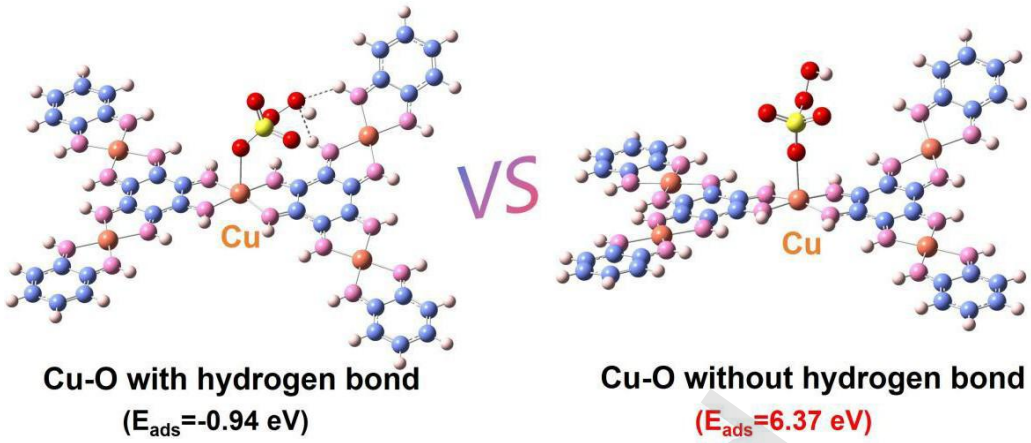

Figure S31. Influence of hydrogen bond on adsorption energy between Cu-HAB and PMS.

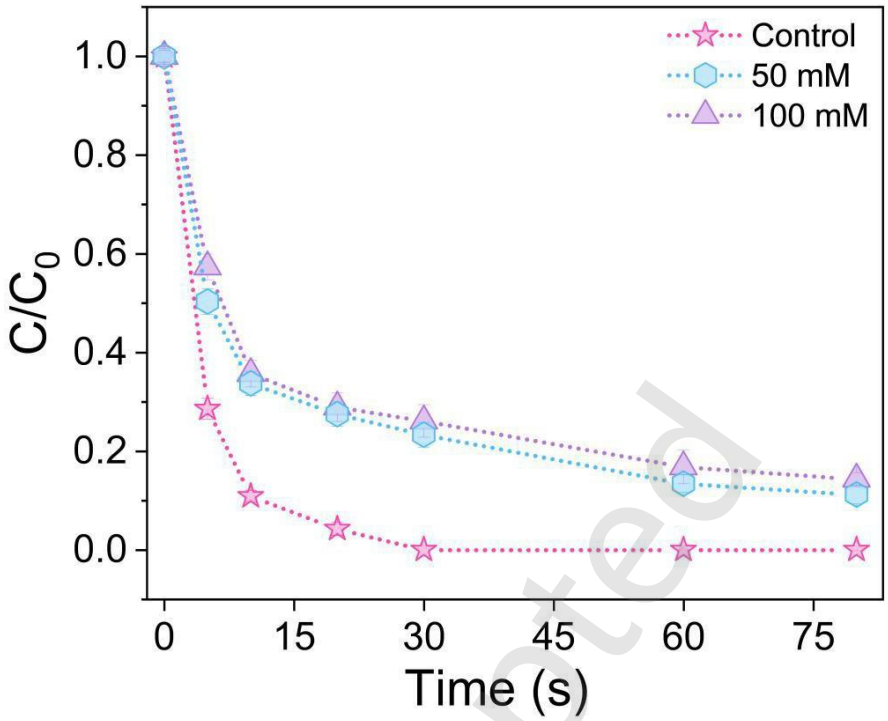

Figure S32. Influence of F^- on 2,4-DCP degradation efficiencies in Co-HAB/PMS system. The error bars in the figures represented the standard deviations from triplicate tests.

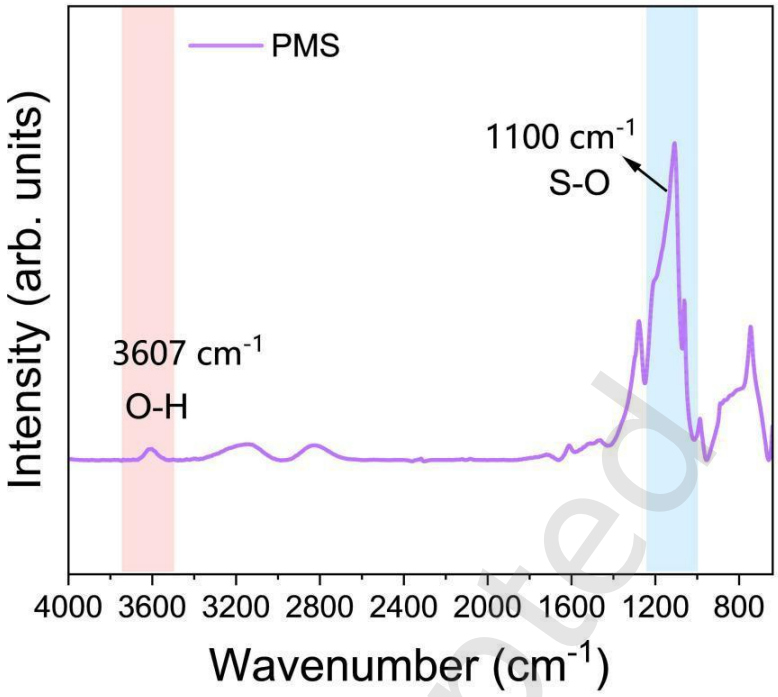

Figure S33. The In-situ FTIR spectrum of individual PMS.

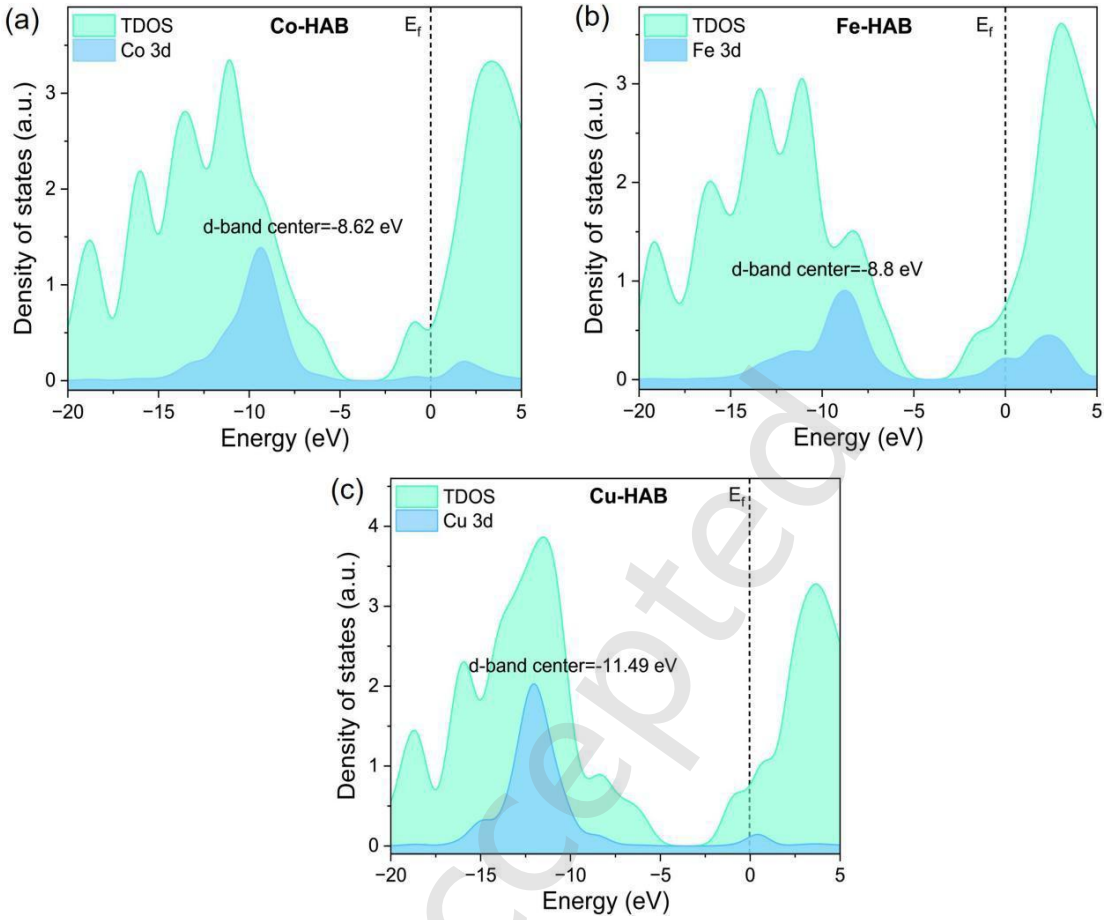

Figure S34. The density of states of Co-HAB, Fe-HAB and Cu-HAB. And the partial density of states of (a) Co element, (b) Fe element and (c) Cu element.

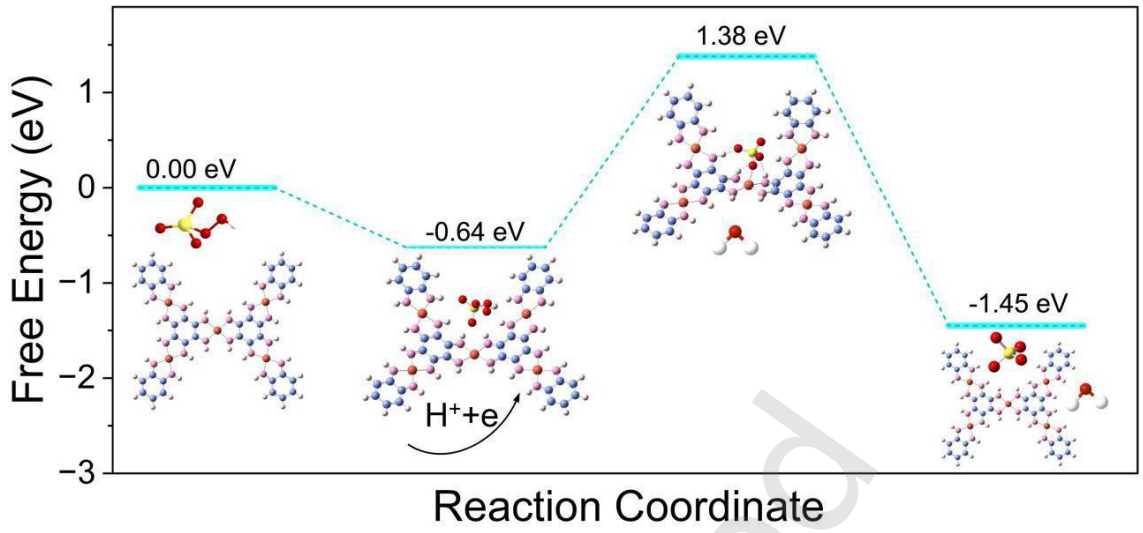

Figure S35. Energy level diagram of $SO_4^{\bullet-}$ production by Co-HAB.

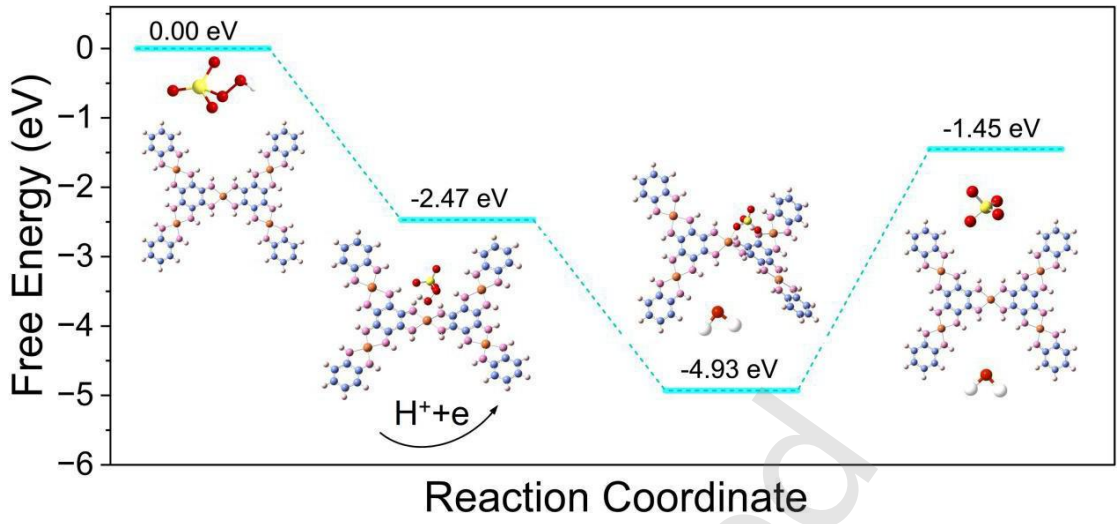

Figure S36. Energy level diagram of $SO_4^{\bullet-}$ production by Fe-HAB.

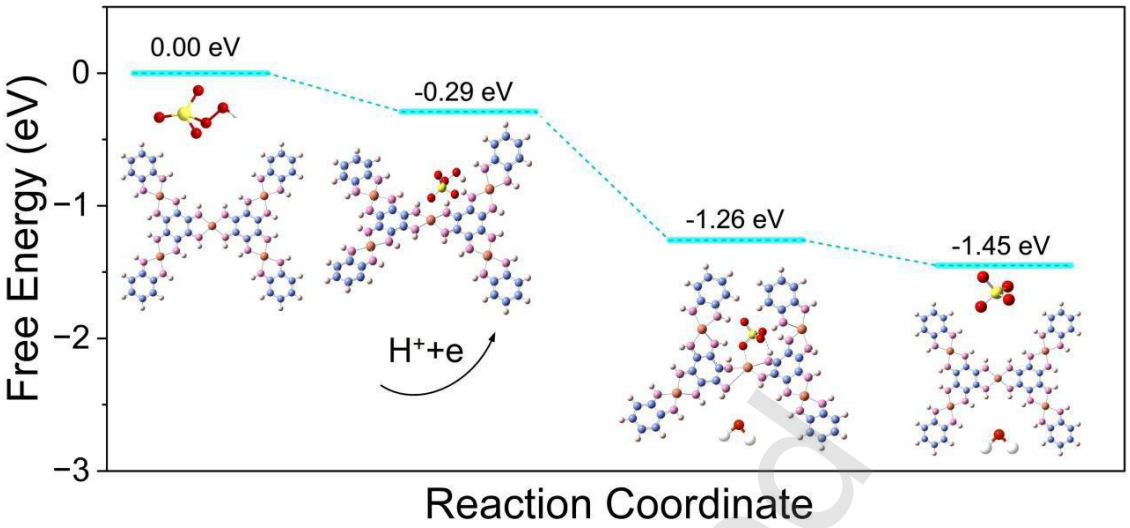

Figure S37. Energy level diagram of $SO_4^{\bullet-}$ production by Cu-HAB.

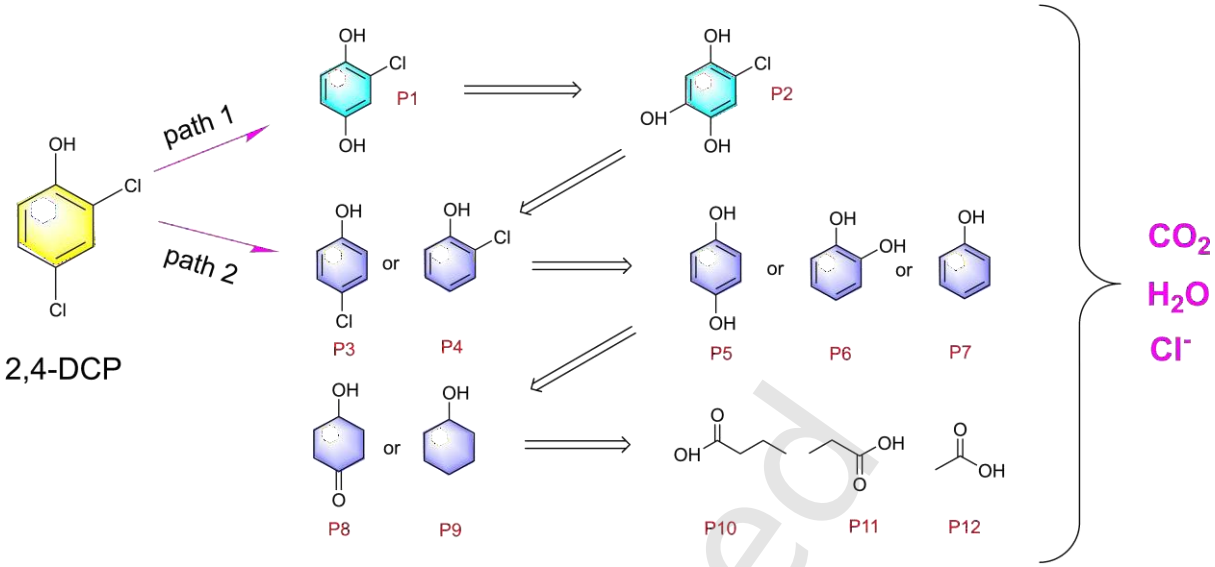

Figure S38. The proposed degradation pathways of 2,4-DCP in this system.

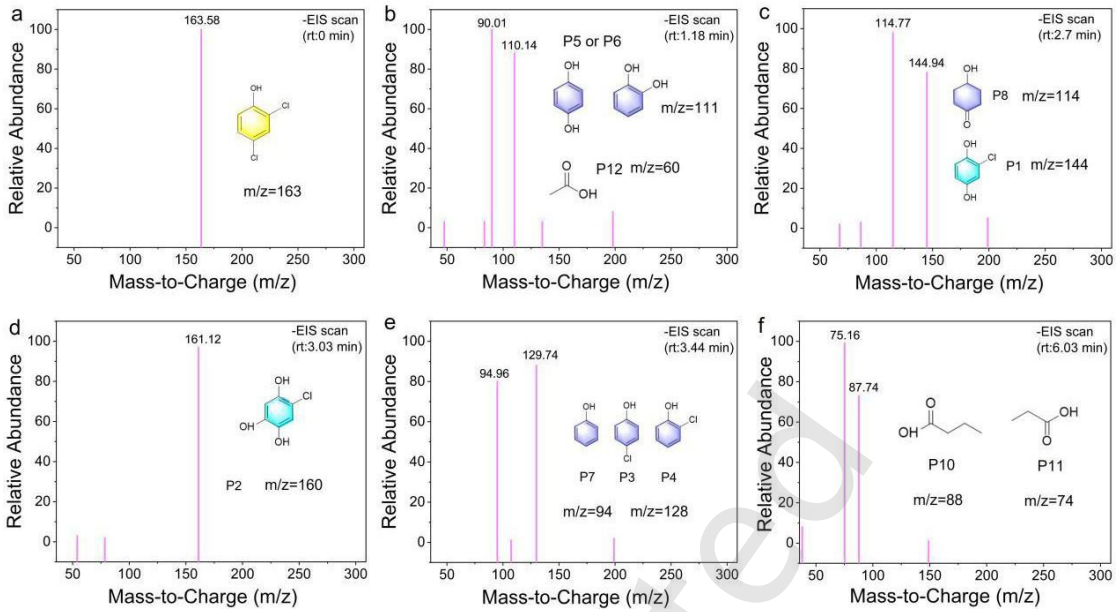

Figure S39. Structure analysis of intermediates. The m/z values of the intermediates of 2,4-DCP degradation determined by LC-MS and corresponding structural formulas: (a) 0 min and (b-f) 10 min.

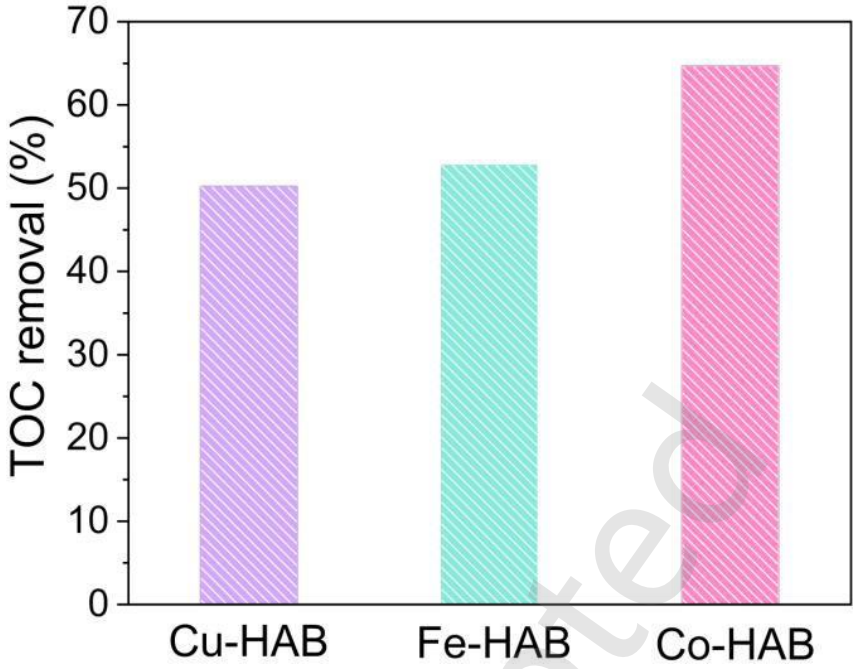

Figure S40. Total organic carbon (TOC) removal measurement by M-HAB systems.

Figure S41. Photo of the catalytic column equipment.

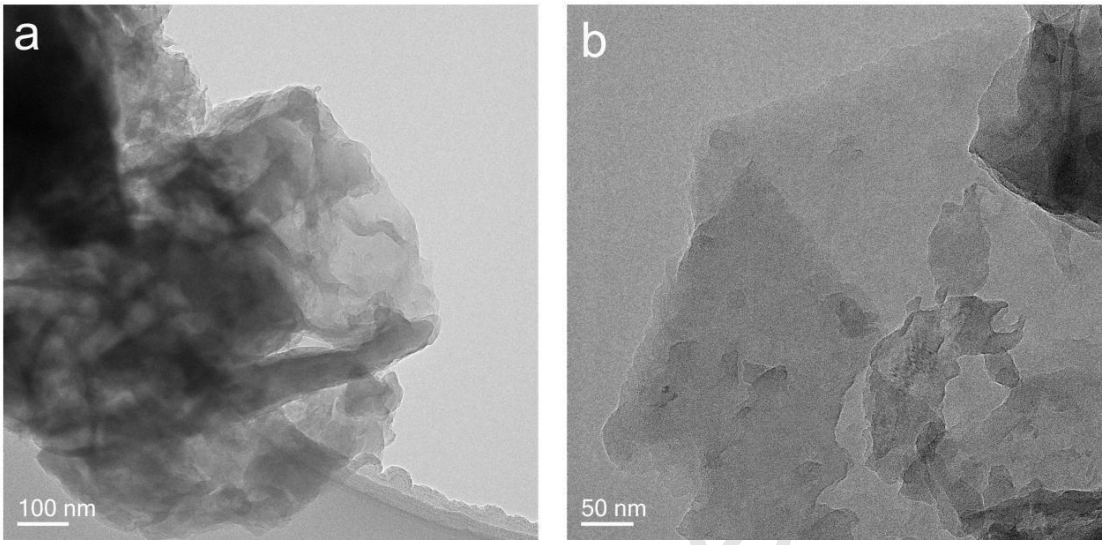

Figure. S42. TEM images of the Co-HAB sample after reaction.

Note: The TEM images show unchanged morphology of the Co-HAB catalyst afterreaction, indicating its high structural stability.

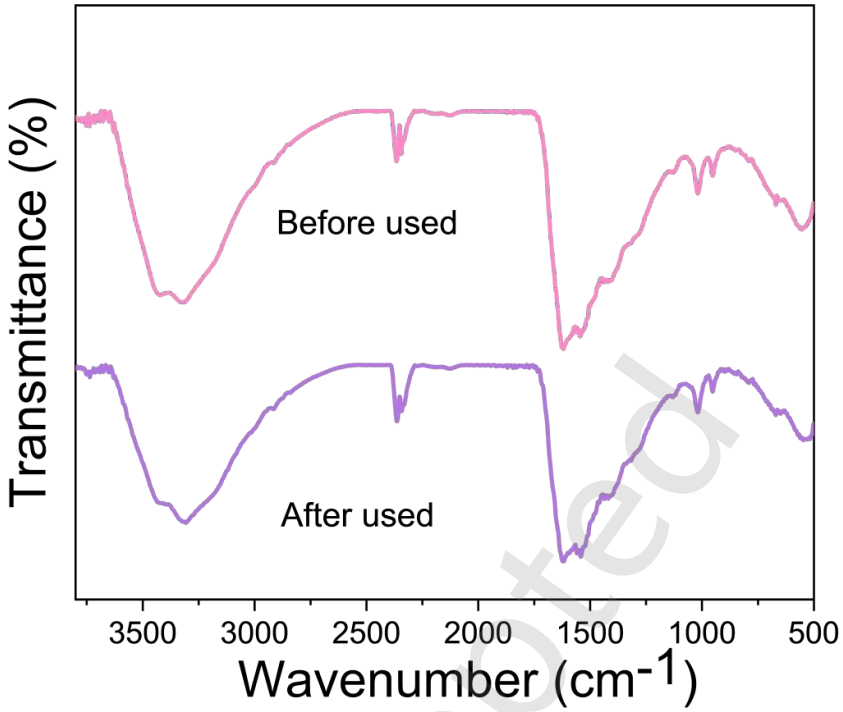

Figure. S43. The FT-IR spectrum of the used Co-HAB.

Tables S1-S5.

Table S1. Content of metal obtained by ICP-OES.

Samples	Metal amounts wt.%
Fe-HAB	7.2
Co-HAB	7.5
Cu-HAB	7.7

Table S2. Analytical details for pollutants by HPLC.

Pollutants	Mobile phase	Ratio	Flow rate (min L^{-1})	Detection (nm)
2,4-DCP	MeOH/H_2O	80:20	1	286
BPA	MeOH/H_2O	70:30	1	276
CBZ	MeOH/H_2O	70:30	1	280
APAP	Ammonium acetate/MeOH	85:15	1	257
PE	MeOH/H_2O	60:40	1	270
ATZ	MeOH/H_2O	70:30	0.8	225
NBA	Acetonitrile/H_2O (0.1% phosphoric acid)	50:50	1	254

Table S3. Comparison of the kinetics of organic contaminant degradation in recently reported Fenton-like processes.

Catalyst (g L^{-1})	Oxidant (mM)	Pollutant	Removal efficiency	k_{obs} (min^{-1})	k-value (min^{-1} M^{-1})	Mechanism	Stability	Ref.
Co-HAB	0.2	2,4-DCP	100% (30 s)	9.25	9250	ETP	700 h	This work
Fe-HAB	0.2	2,4-DCP	100% (4 min)	1.02	1020	ETP, $SO_4^{\bullet-}$	700 h	This work
Cu-HAB	0.2	2,4-DCP	100% (7 min)	0.98	980	$SO_4^{\bullet-}$	700 h	This work
FeCo-DAC	0.4	BPA	100%(15 min)	0.23	57.5	ETP	5 cycles	[8]
CoNBC600	0.5	APAP	100% (11 min)	0.46	92	ETP	10 h	[9]
Fe─N/Cl	3	Acyclovir	100% (25 min)	0.138	27.6	ETP	240 h	[10]
Fe@N-C-800	1	Sulfamethoxazole	100% (6 min)	0.818	16.36	•OH	1.65×10^5 bed volume	[11]
Co-N_3O_1	1	Ciprofloxacin	100%(20 min)	0.287	14.35	$^1O_2$	10 h	[12]
NiCoMn/GO	0.2	Ciprofloxacin	99% (30 min)	0.17	37.57	•OH, $O_2^{\bullet-}$, $SO_4^{\bullet-}$	5 cycles	[13]
I-NC	1	Ciprofloxacin	100%(10 min)	0.436	217.75	$^1O_2$	720 h	[14]
Cu-In_2O_3/O_v	1	Tetracycline	100%(20 min)	0.256	10.24	•OH, $SO_4^{\bullet-}$	25 h	[15]
Fe-N_2	1	Sulfamethoxazole	100%(60 s)	5.28	502	Fe^{IV}=O	/	[16]

MIL-101/ZIF-67 x	1.97	2-CP	90%(10 min)	0.241	305.83	$^1O_2$	5 cycles	[17]
Cu/Zn-ZIF	0.66	BPA	99.5%(60min)	0.098	371	•OH, $SO_4^{\bullet-}$	/	[18]

*: $k\text{-value}=\frac{\text{ko}}{c[\text{Catalyst}]*c[\text{PMS}]}*c[\text{Pollutent}]$

The modified kinetic rate constant (k-value) for the degradation of pollutant was determined by normalizing the observed rate constant to the catalyst dosage and oxidizing agent concentration, and subsequently scaling it with the concentration of pollutant. The Co-HAB/PMS, Fe-HAB/PMS and Cu-HAB/PMS systems demonstrated a remarkable efficiency, 100% degradation of 2,4-DCP within 6 min. The performance were quantified by a notably high k-value of 9250,1020 and 980 min^{-1} M^{-1}, respectively, which notably exceeded the values reported for previously studied catalysts.

Table S4. The bond lengths of N-H bonds in each material before and after the formation of hydrogen bonds.

Catalyst	The bond lengths of N-H bonds before hydrogen bonds formation	The bond lengths of N-H bonds after hydrogen bonds formation
Co-HAB	1.009	1.012
	1.009	1.012
	1.012	1.014
Fe-HAB	1.011	1.014
	1.010	1.013
	1.011	1.012
Cu-HAB	1.010	1.012
	1.011	1.013

Note: In all three materials, the N-H bonds involved in hydrogen bonds have become longer.

Table S5. Change of natural charge of PMS model before adsorption and afteradsorption.

Atom	S1	O2	O3	O4	O5	O6	H7
PMS	2.447	-0.495	-0.965	-1.016	-0.964	-0.459	0.453
PMS-Co-HAB	2.482	-0.511	-0.95	-0.962	-0.926	-0.474	0.479
PMS-Fe-HAB	2.490	-0.499	-0.912	-0.979	-0.922	-0.455	0.470
PMS-Cu-HAB	2.482	-0.509	-0.925	-0.983	-0.954	-0.458	0.467

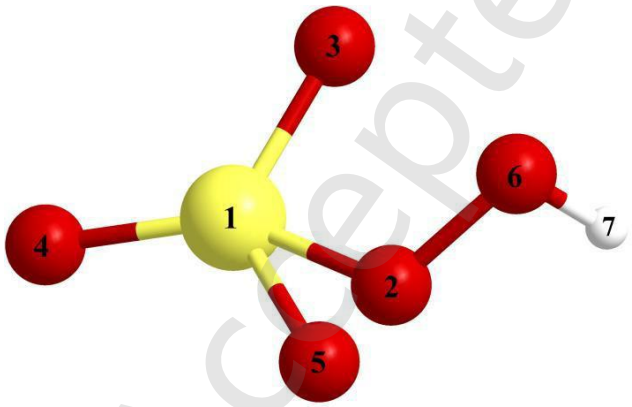

Note: PMS adsorption on materials via terminal O(5).

Supplementary References

[1] Wang, F.; Gao, Y.; Fu, H.; et al.Almost 100 % electron transfer regime over FeCo dual-atom catalyst toward pollutants removal: Regulation of peroxymonosulfate adsorption mode. Appl. Catal. B-Environ. Energy, 2023, 339, 123178.

[2] Chai, J., Head-Gordon, M., " Long-range corrected hybrid density functionals with damped atom-atom dispersion corrections," Phys. Chem. Chem. Phys., 2008, 10, 6615-20.

[3] Dolg, M., Wedig, U., Stoll H., and Preuss, H., "Energy-adjusted ab initio pseudopotentials for the first row transition elements," J. Chem. Phys., 1987, 86, 866-72.

[4] M. J. Frisch, G. W. Trucks, H. B. Schlegel, G. E. Scuseria, M. A. Robb, J. R. Cheeseman, G. Scalmani, V. Barone, G. A. Petersson, H. Nakatsuji, X. Li, M. Caricato, A. V. Marenich, J. Bloino, B. G. Janesko, R. Gomperts, B. Mennucci, H. P. Hratchian, J. V. Ortiz, A. F. Izmaylov, J. L. Sonnenberg, D. Williams-Young, F. Ding, F. Lipparini, F. Egidi, J. Goings, B. Peng, A. Petrone, T. Henderson, D. Ranasinghe, V. G. Zakrzewski, J. Gao, N. Rega, G. Zheng, W. Liang, M. Hada, M. Ehara, K. Toyota, R. Fukuda, J. Hasegawa, M. Ishida, T. Nakajima, Y. Honda, O. Kitao, H. Nakai, T. Vreven, K. Throssell, J. A. Montgomery, Jr., J. E. Peralta, F. Ogliaro, M. J. Bearpark, J. J. Heyd, E. N. Brothers, K. N. Kudin, V. N. Staroverov, T. A. Keith, R. Kobayashi, J. Normand, K. Raghavachari, A. P. Rendell, J. C. Burant, S. S. Iyengar, J. Tomasi, M. Cossi, J. M. Millam, M. Klene, C. Adamo, R. Cammi, J. W. Ochterski, R. L. Martin, K. Morokuma, O. Farkas, J. B. Foresman, and D. J. Fox, Gaussian 16, Revision A.03, Gaussian, Inc., Wallingford CT, 2016.

[5] Lu, T., Chen, F.; Multiwfn: A Multifunctional Wavefunction Analyzer, J. Comput. Chem. 2012, 33, 580-592.

[6] Lu, T., A comprehensive electron wavefunction analysis toolbox for chemists. Multiwfn, J. Chem. Phys., 2024,161, 082503.

[7] Fuster, F., Silvi, B., Does the topological approach characterize the hydrogen bond? Theor Chem Acc 2000, 104, 13-21.

[8] Wang, F.; Gao, Y.; Fu, H.; Liu, S.-S.; Wei, Y.; Wang, P.; Zhao, C.; Wang, J.-F.; Wang, C.-C. Almost 100 % electron transfer regime over Fe-Co dual-atom catalyst toward pollutants removal: Regulation of peroxymonosulfate adsorption mode. Appl. Catal. B-Environ. Energy 2023, 339,123178.

[9] Meng, H.; Zhou, J.; Zhang, Y.; et al. Single-atom Co-N_3 sites induce peroxymonosulfate activation for acetaminophen degradation via nearly 100 % internal electron transfer process. Appl. Catal. B-Environ. Energy 2025, 366, 125038.

[10] Ren, S.; Wang, Y.; Shi, L.; et al. Transforming Plastics to Single Atom Catalysts for Peroxymonosulfate Activation: Axial Chloride Coordination Intensified Electron Transfer Pathway. Adv. Mater. 2024, 2415339.

[11] Wang, L.; Rao, L.; Ran, M.; A polymer tethering strategy to achieve high metal loading on catalysts for Fenton reactions. Nat. Commun. 2023, 14, 7841.

[12] Wang, Z.; Almatrafiet, E.; Wang, H.; et al. Cobalt Single Atoms Anchored on Oxygen-Doped Tubular Carbon Nitride for Efficient Peroxymonosulfate Activation: Simultaneous Coordination Structure and Morphology Modulation. Angew. Chem. Int. Ed. 2022, 61, e202202338.

[13] Nguyen, T.; Le, V.; Huang, C.; et al. Construction of ternary $NiCo_2O_4$/MnOOH/GO composite for peroxymonosulfate activation with enhanced catalytic activity toward ciprofloxacin degradation. Chem. Eng. J. 2022, 446, 137326.

[14] Pei, J.; Liu, J.; Fu. K.; et al. Non-metallic iodine single-atom catalysts with optimized electronic structures for efficient Fenton-like reactions. Nat. Commun. 2025, 16, 1.

[15] Zhao, Z.; Wang, P.; Song, C.; et al. Enhanced Interfacial Electron Transfer by Asymmetric Cu-O_v-In Sites on In_2O_3 for Efficient Peroxymonosulfate Activation. Angew. Chem. Int. Ed. 2023, 62, e202216403.

[16] Lin, Y.; Wang, Y.; Weng, Z.; et al. Coordination engineering of heterogeneous high-valent $Fe^{(IV)}$-oxo for safe removal of pollutants via powerful Fenton-like reactions .Nat. Commun. 2024, 15, 10032.

[17] Gu, A.; Wang, P.; Chen, K.; et al. Core-shell bimetallic Fe-Co MOFs to activated peroxymonosulfate for efficient degradation of 2-chlorophenol. Sep. Purif. Technol. 2022, 298.

[18] Yin, R.; Zhou, X.; Shi, Y.; et al. ZIF-derived non-bonding Cu/Zn catalysts-driven peroxymonosulfate activation via selective generation of surface-bound radicals for efficient water purification. Chem. Eng. J. 2024, 501, 157592.